الجمهورية الجزائرية الديمقراطية الشعبية
The People's Democratic Republic of Algeria
وزارة التعليم العالي والبحث العلمي
Ministry of Higher Education and Scientific Research
جامعة الشهيد حمه لخضر - الوادي
University of Echahid Hamma Lakhdar - El-Oued
كلية العلوم الدقيقة
Faculty of Exact Sciences
قسم الكيمياء
Department of Chemistry

Thesis for obtaining the doctorate degree in Analytical Electrochemistry and Environment

Thesis title:

Synthèse et caractérisation physicochimique des oxydes de structure spinelle

Synthesis and Physicochemical Characterization of $ZnFe_{2-x}Ni_xO_4$ & $Y_{1-x}Cu_xO_3$ for photocatalysis application

Prepared by: Miss Jannat Hammouche

Defence date: 15/12/2022

Doctoral advisory committee members:

Mr Touhami Lanez	Prof.	Univ. El-Oued	President
Mr Mahmoud Omari	Prof.	Univ. Biskra	Supervisor
Mr Djamel Barkat	Prof.	Univ. Biskra	Examinator
Mr. Mohammed Ridha Ouahrani	Prof.	Univ. El-Oued	Examinator
M^{me}. Naima Benchikha	Prof.	Univ. El-Oued	Examinator
Mr Mohamed Dhamchia	Prof.	Univ. El-Oued	Examinator
Mr Mounir Gaidi	Prof.	Univ. Sharjah UAE	Invited

University year:
2022/2023

Gratitude & Aknowldgement

I would like to express my deepest appreciation to everyone who contributed to my PhD research and helped me attain the momentous achievement of defending my thesis in 15th of December 2022, after many years of struggle and patience. First and foremost, I want to thank my family, especially my parents, for their constant support, continuous encouragement, wise words, and passionate prayers kept me going. Despite the various difficulties and times of feeling defeated, I experienced along the journey. I am also grateful to my siblings, who have faith in me as their elder sister worked as an endless motivator.

Furthermore, I would like to offer my sincere gratitude to everyone I met, I contributed and dealt with throughout my time at the University of Sharjah in the United Arab Emirates from 2019 to 2022:

- Professor Hussain Alawadhi, who welcomed me to the Center of Advanced Materials and Research Labs, gave me access to the facilities I needed.
- Professor Mounir Kaidi, whose guidance, supervision, and regular advice had a significant impact on the progress of my research.
- Professor Tarek Merabtine "Responsible of the International Relations Office", whose strong help and good counsel supported me in resolving a variety of problems that I faced. I would also wish to thank his secretary, Moza Alsuwaidi, for her important assistance.
- Dr. Soumya, a great friend and trustworthy source of help during my thesis research.
- Dr. Kais Daoudi, whose constant support and encouragement was vital in driving me to finish my PhD studies.
- Mohamed Shameer, Muhammad Adil Abbasi, Muhammed Irshad, Najrul Hussain, Fahad Hassan, and Ahmed Bahaa, the lab engineers who worked hard to characterize my samples. I would also appreciate all the people I met and involved with, including Rania Ziad Ghabboun, Krithikadevi Ramachandaran, Mikail Pylnev, Halima Alnaqbi, and Maham Sohail.
- Huriah Aljabri, Athbah Nawaf, Marwa Hamada, Aisha Alalwi, the sisters Rufayda & Symaya abdrexit, and Maria Abubaker were among my dearest university dorm close friends.

Mostly, I would thank my Algerian friends: my dearest friend Sara Diab for her strong belief in my ability to achieve my dreams, Nabila Cherifi, Asma Bahdaouia, and Souhaila Bouamor for their support and their precious advices.

Last but not least, I am grateful to my supervisor, Professor Mahmoud Omari, for his endless guidance and support during the years of research, as he carefully guided me toward the successful completion of my thesis.

At last, I want to express my gratitude to the members of the jury who generously accepted to be members of my defence's advisory committee: Professor Touhami Lanez, Professor Djamel Barkat, Professor Mohammed Ridha Ouahrani, Professor Naima Benchikha, and Professor Mohamed Dhamchia.

I sincerely apologize to everyone whose names were unintentionally not mentioned.

Jannat Hammouche

Table of Contents

List of titles & pages

Part A: Bibliography

Part B: Experimental and application

Abstract

Abbreviations

ZFO: $ZnFe_2O_4$

YFO: $YFeO_3$

List of Figures

List of tables

Disclaimer:

-The percentage of plagiarism existed in literature review part (general introduction and part A: bibliography) is 11% according to turnitin.

-While checking the percentage of plagiarism you should remove the list of references and exclude the phrases between double quotes from the document so the report of plagiarism will be accurate.

-We checked the percentage of plagiarism for literature review only because the experimental part is our work and the Journal allowed us to added it to the thesis and the last chapter is sent to the journal and we are waiting to their response about it.

تنويه:

- نسبة الاقتباس الموجودة في الجزء النظري (المقدمة العامة والجزء أ: بيبلوغرافيا) هي 11٪ حسب تيرنتين.
- خلال تفقد نسبة الاقتباس يجب حذف قائمة المراجع وكذلك اسثناء الجمل الموجودة بين " " من الملف كي تكون نسبة الاقتباس دقيقة.
- تم قياس نسبة الاقتباس للجزء النظري فقط لأن الجزء التجريبي هو عملنا الخاص والمجلة سمحت لنا بإضافته إلى المذكرة والفصل الأخير تم إرساله للمجلة في انتظار الرد منهم.

General introduction

General introduction

A_2BO_4 spinel and ABO_3 Perovskite oxides are significant functional materials due to their wide range of crystal structures and stoichiometries, they could incorporate almost 90% of the natural metallic elements at the A and/or B positions that stand fully or partially without disrupting the lattice structure, allowing solid-state chemistry to be linked to catalytic characteristics [1]. Furthermore, the desired textural structure and physicochemical properties; “their high thermal and hydrothermal stability makes them suitable catalytic materials”, can be achieved by the preparation process [2].

On one side, many investigations were directed to the synthesis and characteristics of spinel nano oxide systems in order to fulfil the essential need for higher chemical and thermal stabilities with promising catalytic and photocatalytic activities [3]. As a result, the spinel ferrites nanomaterials provide one of the most varied environmental experiments to investigate their physical properties, and fundamental and applied behavior [4]. The space group Fd3m contains the majority of spinel compounds [5]. Whereas $ZnFe_2O_4$ (ZFO) is a major ferrite binary oxide with a spinel structure [6]. $ZnFe_2O_4$ has a typical spinel structure, where Zn^{2+} ions and Fe^{3+} ions at the tetrahedral and the octahedral sites respectively. Although, nanosized $ZnFe_2O_4$ nanoparticles can also exhibit cationic inversion, and both cations of Zn^{2+} and Fe^{3+} ions locate on both sites is related to the preparation method of spinel ferrite nanoparticles [7]. The Fe-d orbitals affectsignificantly on the magnetic, electrical and photocatalytic properties of ZFO [8, 9]. Herein, the microstructure and the stoichiometric of ZFO nanoparticles determine their physicochemical properties [10]. In addition, cationic redistribution, size and shape homogeneity, as well as structural, optical, electrical, and magnetic properties are all strongly influenced by synthesis methods [11]. There are various preparation methods for the synthesis of spinel ferrite nanoparticles, such as [12] “solid-state reaction (SSR) method, microwave, sol-gel, co-precipitation, hydrothermal method, hydrothermal–microwave method, solvothermal, pyrolysis method [13-16], reverse-micelle method, combustion method, sonochemical method, high energy ball milling,” etc... One of these synthesis methods, the “sol-gel auto-combustion process” [17] is used to accelerate the synthesis of complex materials. It is a simple process that saves time and energy over traditional methods while also requiring a lower sintering temperature. This method is used to improve the powder properties, homogeneity, and particle size distribution of spinel ferrites, thereby influencing their structural, electrical, and magnetic properties [18]. The type of fuel used can affect the reaction during a combustion method. Citric acid, urea, and glycine are some of the most widely utilized fuels for the combustion synthesis of spinel ferrite nanoparticles [19]. Because Spinel oxides can be synthesized in each size and geometry based on the desired application due to their flexible physical and chemical characteristics [18].

On the other side, orthoferrites nano-powders with Perovskite structure ABO_3 got the interest for technological applications in medical, water splitting and plenty of other fields of engineering, magneto-optical devices, fuel cells, battery, sensors, and photocatalysis; due to the fact of its promising multiferroic properties and abnormal chemical and physical behaviors [20-25]. Furthermore, the Yttrium orthoferrite exhibits promising magnetic properties due to the interactions between the Fe ions [22, 23]. Though, under visible light, the semiconductor $YFeO_3$ has an excellent photocatalytic behavior degrading organic dyes compared to TiO_2 due to its narrow bandgaps; E_g (o-$YFeO_3$) ≥ 2.1 eV and E_g (h-$YFeO_3$) = 1.81 eV [25-27]. Since the Yttrium orthoferrite is influenced by the preparation method, combustion methods such as Glycine Nitrates Process (GNP) were a great option to obtain nanosized orthoferrite with narrow distribution particles due to its simplicity and no need for several steps, short time of synthesis, and getting pure crystalline products and sometimes no need of sintering, even though it can lead to the appearance of new phases in the structure, dopants incorporate into the final products of the desired composition in a good chemical homogeneity of the cations [27, 28]. Also, the substitution effect on the A site or B site of $YFeO_3$ has improved its properties and enlarged the range of its applications [20, 24].

Hence, the photocatalytic behavior of one-dimensional (1 D) $YFeO_3$ was not studied before the reported work of Zhang, Ruslan, et al. [29], and fewer photocatalytic activity studies under visible light were done on the $YFeO_3$ nanopowders but no studies were done yet under UV light.

The photocatalytic activity of the Yttrium ferrite got the interest of researchers under visible light as an excellent alternative to TiO_2 and it gives a good degradation efficiency with the decrease of the crystallite size [30].

In this thesis, we divided our work into two parts; part A is for the bibliographic review in brief about Spinel and Perovskite oxides; Zinc and Yttrium ferrites, the characterization and synthesis methods, and the concept of photocatalysis. Whereas Part B is for the experimental work, the discussion of obtained results, and the photocatalysis application.

References

1. Junjiang Zhu et al, Perovskite Oxides: Preparation, Characterizations, and Applications in Heterogeneous Catalysis, American Chemical Society, 2014.

2. Huo, J., Tessonnier, J. P., & Shanks, B. H. (2021). Improving hydrothermal stability of supported metal catalysts for biomass conversions: A review. *ACS Catalysis*, *11*(9), 5248-5270.

3. T. Tatarchuk et al. “Catalytic and Photocatalytic Properties of Oxide Spinels”, L. M. T. Martínez et al. (eds.), Handbook of Eco materials, 2018.

4. Sickafus, K. E., Wills, J. M. and Grimes, N. W., Structure of spinel. J. Am. Ceram. Soc., 1999, 82(12), 3279–3292.

5. Maletin, M., Cvejic,´ Z., Raki ˇ c, S., Nikoli ´ c, Lj. M. and Srdi ´ c, V. V., Low- ´ temperature synthesis of nanocrystalline ZnFe2O4 powders. Mater. Sci. Forum, 2006, 518, 91–94.

6. H.H. Hamdeh, J.C. Ho, S.A. Oliver, R.J. Willey, G. Oliveri, G. Busca, J. Appl. Phys. 81 (1997) 1851–1857., [4] S.A. Oliver, H.H. Hamdeh, Phys. Rev. B 60 (1999) 3400–3405.

7. R. S. Yadav, J. Havlica, J. Masilko, J. Tkacz “Anneal-tuned structural, dielectric and electrical properties of ZnFe2O4 nanoparticles synthesized by starch-assisted sol-gel auto-combustion method”, J Mater Sci: Mater Electron, 2016.

8. Dom R, Subasri R, Radha K, Borse PH. Synthesis of solar active nanocrystalline ferrite, MFe2O4(M: Ca, Zn, Mg) photocatalysts by microwave irradiation. Solid State Communications 2011; 151(6):470–473.–21.

9. Ponpandian N, Narayanasamy A. Influence of grain size and structural changes on the electrical properties of nanocrystalline zinc ferrite. Journal of Applied Physics 2002; 92(5):2770–2778.

10. Sivakumar M, Takani T, Ikuta H, Towata A, Yasui K, Suzuki T, Kozuka T, Bhattacharya D, Iida Y. Fabrication of zinc ferrite nanocrystallites by sonochemical emulsification and evaporation: observation of magnetization and its relaxation at low temperature. Journal of Physical Chemistry B 2006; 110(31):15234–15243.

11. J.F. Xu, W. Ji, Z.X. Shen, S.H. Tang, X.R. Ye, D.Z. Jia, X.Q. Xin, J. Solid State Chem. 147, 516–519 (1999), 23. M. Vaseem, A. Umar, Y.B. Hahn, D.H. Kim, S.K. Lee, J.S. Jang, J.S. Lee, Catal. Commun. 10, 11–16 (2008), 24. R. Sathyamoorthy, K. Maheshwari, Physica E 47, 157–161 (2013).

12. R. S. Yadav, J. Havlica, J. Masilko, J. Tkacz “Anneal-tuned structural, dielectric and electrical properties of ZnFe2O4 nanoparticles synthesized by starch-assisted sol–gel combustion method”, J Mater Sci: Mater Electron, 2016.

13. Dom R, Subasri R, Radha K, Borse PH. Synthesis of solar active nanocrystalline ferrite, MFe2O4(M: Ca, Zn, Mg) photocatalysts by microwave irradiation. Solid State Communications 2011; 151(6):470–473.

14. Dom R, Subasri R, Hebalkar NY, Chary AS, Borse PH. Synthesis of hydrogen-producing nanocrystalline ZnFe2O4 visible light photocatalyst using a rapid microwave irradiation method. Royal Society of Chemistry Advances 2012; 2(33):12782–12789.

15. Jang JS, Hong SJ, Lee JS, Borse PH, Jung OS, Hong TE, Jeong ED, Won MS, Kim HG. Synthesis of zinc ferrite and its photocatalytic application under visible light. Journal - Korean Physical Society 2009; 54(1):204–208.

16. Sun Y, Wang W, Zhang L, Sun S, Gao E. Magnetic ZnFe2O4 octahedra: synthesis and visible-light-induced photocatalytic activities. Materials Letters 2013; 98:124–127.].

17. R. S. Yadav, J. Havlica, J. Masilko, J. Tkacz “Anneal-tuned structural, dielectric and electrical properties of ZnFe2O4 nanoparticles synthesized by starch-assisted sol–gel auto-combustion method”, J Mater Sci: Mater Electron, 2016.

18. Auzans, E., Zins, D., Blums, E., &Massart, R. (1999). Synthesis and Properties of Ferrite.Journal of Materials Science, 34(6), 1253-1260.

19. R. S. Yadav, J. Havlica, J. Masilko, J. Tkacz “Anneal-tuned structural, dielectric and electrical properties of ZnFe2O4 nanoparticles synthesized by starch-assisted sol–gel auto-combustion method”, J Mater Sci: Mater Electron, 2016.

20. Suthar, L., Jha, V. K., Bhadala, F., & Roy, M. (2020). Synthesis, electrical and IR spectroscopy of Calcium substituted Yttrium ferrite ceramics. Materials Today: Proceedings, 26, 3353-3356.

21. Suthar, L., Bhadala, F., & Roy, M. (2019). The impact of Bi3+ substitution for Y3+ cation on the structural, topographical, electrical and thermal behaviour of YFeO3. Ceramics International, 45(16), 20891-20899.

22. Suthar, L., Bhadala, F., Kumari, P., & Roy, M. (2020). Structural, morphological, magnetic and spectral studies of Bi 3+ substituted YFeO 3 Nano-powders: Obtained by sol-gel synthesis. Journal of Electroceramics, 44(3), 195-202.

23. Bharadwaj, P. S. J., Kundu, S., Kollipara, V. S., & Varma, K. B. (2019). Structural, optical and magnetic properties of Sm3+ doped yttrium orthoferrite (YFeO3) obtained by sol–gel synthesis route. Journal of Physics: Condensed Matter, 32(3), 035810.

24. Shen, H., Xu, J., Jin, M., & Jiang, G. (2012). Influence of manganese on the structure and magnetic properties of YFeO3 nanocrystal. Ceramics International, 38(2), 1473-1477.

25. Nagrare, B. S., Kekade, S. S., Thombare, B., Reddy, R. V., & Patil, S. I. (2018). Hyperfine interaction, Raman and magnetic study of YFeO3 nanocrystals. Solid State Communications, 280, 32-38.

26. Zhang, C., Wang, X., Wang, Z., Yan, H., Li, H., & Li, L. (2016). Dielectric relaxation, electric modulus and ac conductivity of Mn-doped YFeO3. Ceramics International, 42(16), 19461-19465.

27. Ismael, M., Elhaddad, E., Taffa, D. H., & Wark, M. (2017). Synthesis of phase pure hexagonal YFeO3 perovskite as efficient visible light active photocatalyst. Catalysts, 7(11), 326.

28. Popkov, V. I., & Almjasheva, O. V. (2014). Formation mechanism of YFeO 3 nanoparticles under hydrothermal conditions. Наносистемы: физика, химия, математика, 5(5).

29. Zhang, R., Wang, X., Yu, C., Liu, J., Yao, J., Kang, X., ... & Xiong, S. (2020). Preparation of Multiferroic YFeO3 Nanofibers and the Photocatalytic Activity under Visible Irradiation. Integrated Ferroelectrics, 206(1), 105-111.

30. Asif, M., Khan, M. A., Atiq, S., Alshahrani, T., Mahmood, Q., Kattan, N. A., & Manzoor, A. (2021). Evolution of structure and improvement in dielectric properties of praseodymium substituted YFeO3 nanomaterials synthesized via a sol-gel auto-combustion method. Ceramics International, 47(5), 6663-6674.

Part A: Bibliography

Chapter 1: Spinel and Perovskite structure oxides

A.1.1. Spinel oxides:

Spinel oxides with unique crystal structures [1] may have plenty of attractive magnetic and electric properties that distinguish them from other micro/nanostructured materials, making them suitable for current technology, also they have the prospects to be used in innovative applications: "magnetic drug delivery, ferrofluids, and high-density information storage "[2].

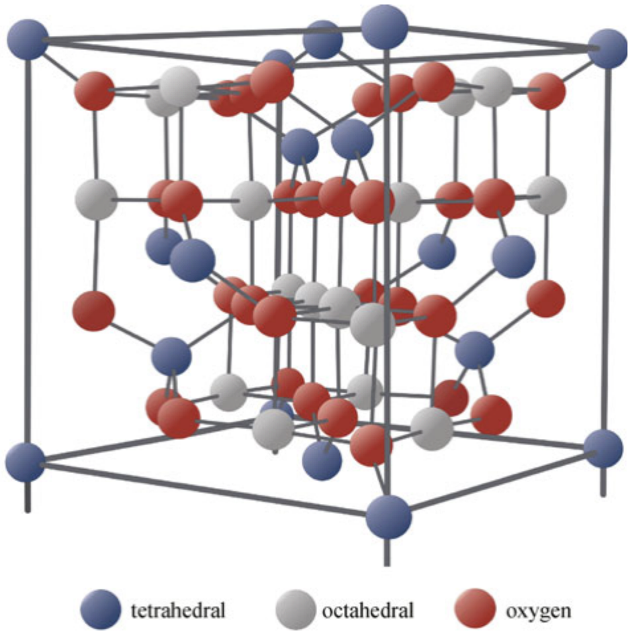

Fig. A.1.1 Representation of spinel structure configuration[2].

Spinel oxides are mostly known that they have a cubic structure with three different types depending on the positions of their cations on which site they are located on [3]. Spinel oxides have a close-packed fcc oxygen atoms configuration with two non-equivalent crystallographic sites A and B with tetrahedral (Th) and octahedral (Oh) coordination [4-6] where the types of Spinel structure are affected by the preparation method, the substitution/doping of metallic elements and their concentration percentage in the structure [7, 8]. AB_2O_4 represented the general formula of the Spinel structure that can be written with this formula $[A_{\mu} B_{1-\mu}]^{Th}[A_{1-\mu} B_{1+\mu}]^{Oh}O_4$ to show their different types; where A is a divalent cation, B is a trivalent cation, O is the oxygen anion, Th is the tetrahedral sites, Oh is the octahedral sites, and μ is the inversion degree in the spinel structure that determines the types of the spinel structure [9], where some examples of the spinel types are shown in the following table:

Table A.1.1 represents types of Spinel Oxides and their structures [10, 11].

$[A_\mu B_{1-\mu}]^T [A_{1-\mu} B_{1+\mu}]^O O_4$	**Degree of inversion μ**	**Tetrahedral site**	**Octahedral site**	**Examples**
Inverse/indirect	$\mu = 0$	1 B	1 A + 1 B	Fe_3O_4, $CoFe_2O_4$
Intermediate/mixed	$0 \leq \mu \leq 1$	$(1 - \mu)$ A + μ B	$(2 - \mu)$ B + μ A	$MgFe_2O_4$
Normal/Direct	$\mu = 1$	1 A	2 B	$MgAl_2O_4$, $MnFe_2O_4$

A.1.1.a. $ZnFe_2O_4$:

The nanoparticle materials have been continuously the study topic of attraction in physics and in other fields [12, 13]. The technological applications use spinel ferrites materials hugely because of their great interest. They allow the theoretical understanding of nanoscale interactions [14-16] in spinel materials is possible. $ZnFe_2O_4$ is particularly intriguing for studying how grain size affects its morphological and magnetic properties [17]. The electronic industry widely utilizes $ZnFe_2O_4$ and its solid solutions with ferrites due to their properties [18].

In its bulk form $ZnFe_2O_4$ follows the spinel structure has solely Zn^{2+} ions in the A sites and Fe^{3+} ions in the B sites. Recent studies on nanocrystalline $ZnFe_2O_4$ have indicated that there is an inversion in cation distribution in this material leading to an anomaly in magnetization [15-17]. Many researchers have reported that nanophase, ZnFe2O4 exhibits ordering with ordering temperatures and a significant magnetic moment [15-17, 19, 20].

Several studies have been conducted on zinc ferrite nanoparticles in years [15, 21, 22]. It is well known that reaction conditions can influence the particle size and morphology of powders. These particle properties greatly impact the material characteristics [22]. Furthermore, the size reduction of a material has been observed to result in properties. These properties can arise from either the volume (known as superparamagnetism) or the high surface, to volume ratio (referred to as spin canting) [21].

Researchers have discovered that particles, with composition exhibit varying magnetic properties depending on the technique used for their preparation [23].

A.1.2. Perovskite Oxides:

The perovskite transition-metal oxides are a flexible crystallographic host formed of formula units ABO_3, where A and B are commonly simple and a transition metal cations, respectively. This structure is exceptionally tolerant of vacancy formation and is highly stable against the replacement of any of the cations. Furthermore, they are true multifunctional high-tech materials for current and future technologies, serving as dielectric resonators, superconductors, microwave dielectrics, and catalysts, as well as key components in sensors, detectors, capacitors, and piezoelectric applications of all types [24].

The crystal structures of many ABO_3 compositions; as we summarized them in table A.2 by their different types.

Table A.1.2: Perovskite structure types, space groups, and lattice parameters.

Perovskite structure type	Space group	Lattice parameters	Examples of structure type	References
Ideal	Pm3m	a = b = c = 3.905 Å and α = β = Ɣ = 90°	$SrFeO_3$ and $SrTiO_3$	[25-27]
Tetragonal	P4mm	a = 3.902 Å, *c* = 4.156 Å	$RbTaO_3$, $PbTiO_3$ and $PbVO_3$	[28, 29]
Rhomboedric	R3c	a = b = 5,365 Å and c = 13,11 Å Angle ≈ 59°	$LaAlO_3$ and $BiFeO_3$	[30, 31]
Orthorhombic	Pnma	a = 5.3458 Å, b = 5.623 Å and c = 7.638 Å	$GdFeO_3$ $GdVO_3$ $CaVO_3$	[29, 32, 33]
Monoclinic	C2/m	-	$RbTaO_3$	[34]
Triclinic	P1	-	$RbNbO_3$	[34]
Hexagonal	$P6_3cm$	-	$SrMnO_3$ $BaMnO_3$	[35]
Polymorphism	-	a' ≈ 4 Å	$BaTiO_3$ $KNbO_3$ $NaSbO_3$	[36, 37]

A.1.3.a. $YFeO_3$:

Because of its unusual magnetic and magneto-optical characteristics, YFeO3 and other rare earth substitution crystals with distorted orthorhombic perovskite-structure (Pbnm) have piqued the interest of researchers since the 1950s. According to Didosyan and colleagues' recent research, orthoferrites show fascinating use in a variety of micro-technological devices such as the measurements of light spot location, magneto-optical current sensors, optical switches, and magnetic field sensors [38-40].

One of the more fascinating elements of the "complex oxide multiferroics–materials" that are both ferroelectric and magnetic is Yttrium orthoferrite. Previously, several "soft chemical techniques" have been used to generate this compound in a nanostructured state [41, 42], including combustion methods [43, 44]. Despite the effective synthesis of yttrium orthoferrite nanoparticles from various starting solutions, it should be emphasised that data about processes leading to the production of $YFeO_3$ nanosized particle, as well as about the influence of synthetic conditions on their final products, are mainly limited [44, 45]. Furthermore, the yttrium cations are located in distorted trigonal prism of O^{2-} anions, and iron cations located in octahedral oxygen environment as shown in the figure.

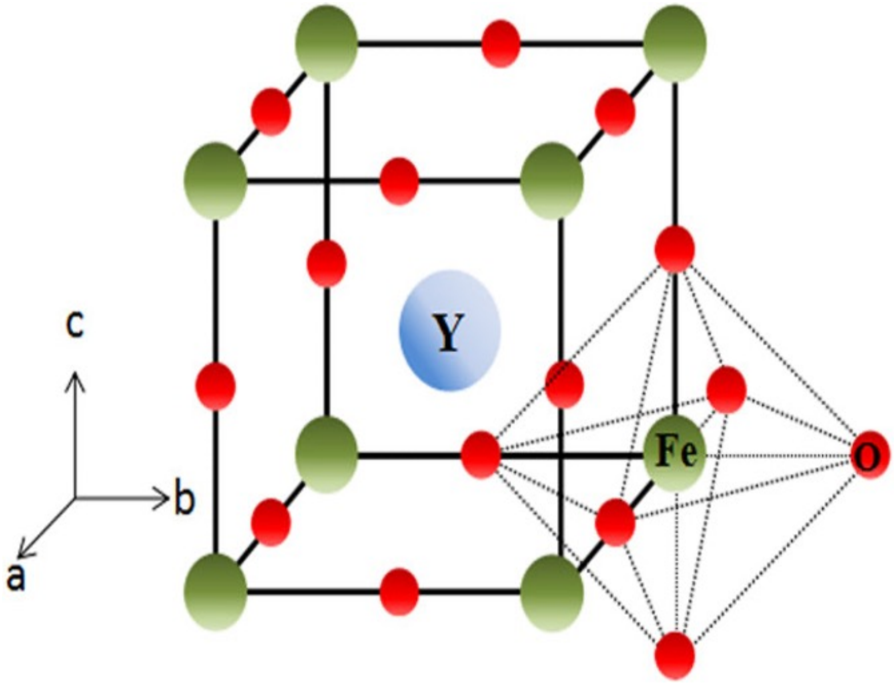

Fig. A.1.2 Representation of the orthorhombic $YFeO_3$ [46].

Besides, The Yttrium orthoferrite, o-$YFeO_3$ is a significant problematic topic under investigation to obtain pure orthorhombic single phase by trying to avoid the appearance of secondary phases such as Y_2O_3, Fe_2O_3, and $Y_3Fe_5O_{12}$ according to the synthesis processes and conditions [47, 48, 49], also thermodynamically, $YFeO_3$ is a polymorphism orthorhombically unstable and hard to obtain it where a hexagonal structure h-$YFeO_3$ can be formed too due to its stability [50-53].

References

1. Wei, R., Bu, X., Gao, W., Villaos, R. A. B., Macam, G., Huang, Z. Q., ... & Ho, J. C. (2019). Engineering surface structure of spinel oxides via high-valent vanadium doping for remarkably enhanced electrocatalytic oxygen evolution reaction. *ACS applied materials & interfaces*, *11*(36), 33012-33021.
2. Sutka, A., & Mezinskis, G. (2012). Sol-gel auto-combustion synthesis of spinel-type ferrite nanomaterials. *Frontiers of Materials Science*, *6*(2), 128-141.
3. Zakaria, A. K. M., Nesa, F., Khan, M. S., Datta, T. K., Aktar, S., Liba, S. I., ... & Eriksson, S. G. (2015). Cation distribution and crystallographic characterization of the spinel oxides MgCrxFe2− xO4 by neutron diffraction. *Journal of Alloys and Compounds*, *633*, 115-119.
4. Hosterman, B. D. (2011). Raman spectroscopic study of solid solution spinel oxides.
5. Jacob, K. T., & Alcock, C. B. (1977). Activities and their relation to cation distribution in NiAl2O4 MgAl2O4 spinel solid solutions. *Journal of Solid State Chemistry*, *20*(1), 79-88.
6. Wei, S. H., & Zhang, S. B. (2001). First-principles study of cation distribution in eighteen closed-shell A II B 2 III O 4 and A IV B 2 II O 4 spinel oxides. *Physical Review B*, *63*(4), 045112.
7. Hassan, M. A., Mamat, O. B., & Mehdi, M. (2020). Influence of alloy addition and spinel coatings on Cr-based metallic interconnects of solid oxide fuel cells. *International Journal of Hydrogen Energy*, *45*(46), 25191-25209.
8. An, L., Hu, Y., Li, J., Zhu, J., Sun, M., Huang, B., ... & Yan, C. H. (2022). Tailoring Oxygen Reduction Reaction Pathway on Spinel Oxides via Surficial Geometrical-Site Occupation Modification Driven by the Oxygen Evolution Reaction. *Advanced Materials*, *34*(28), 2202874.
9. Zhu, J., Li, H., Zhong, L., Xiao, P., Xu, X., Yang, X., ... & Li, J. (2014). Perovskite oxides: preparation, characterizations, and applications in heterogeneous catalysis. *Acs Catalysis*, *4*(9), 2917-2940.
10. Szotek, Z., Temmerman, W. M., Ködderitzsch, D., Svane, A., Petit, L., & Winter, H. (2006). Electronic structures of normal and inverse spinel ferrites from first principles. *Physical Review B*, *74*(17), 174431.
11. Vedrtnam, A., Kalauni, K., Dubey, S., & Kumar, A. (2020). A comprehensive study on structure, properties, synthesis and characterization of ferrites. *AIMS Materials Science*, *7*(6), 800-835.
12. Edelstein A S & Cammarata R C (Eds), Nanomaterials: synthesis, properties and applications (Institute of Physics Publishing, Bristol), 1998.
13. Louis Bros, J Phys Chem Solids, 59 (1998) 459.
14. Upadhyay C, Verma H C, Rath C, Sahu K K, Anand S, Das R P & Mishra N C, J Alloys Compd, 326 (2001) 94.
15. Anantharaman M R, Jagatheesan S, Malini K A, Sindhu S, et al., J Magn Magn Mater, 189 (1998) 83.
16. Chinnasamy C N, Narayanasamy A, Ponpandian N, Chattopadhyay K, Guerault H & Grenache J M, Scripta Mater, 44 (2001) 1407.
17. Chinnasamy C N, Narayanasamy A, Ponpandian N, Chattopadhyay K, Guerault H & Grenache J M, J Phys Condens Matter, 12 (2000) 7795.
18. Jiang J S, Yang X L, Gao L & Jiang J Z, Nanostruct Mater, 12 (1999) 143.
19. Mohai I, Szepvolgyi J, Bertoti I, Mohai M, Gubicza J & Ungar T, Solid State Ionics, 141-142 (2001) 163.
20. Yuan Zhihao & Zhang Lide, Mater Res Bull, 33 (1998) 1587.

21. Sato T, Haneda K, Seki N & Iijjma T, Appl Phys A, 50 (1990) 13.
22. Hamdeh H H, Ho J C, Oliveri S A, Willey R J, Oliver G & G. Busca G, J Appl Phys, 81 (1997) 1851.
23. Ziuling Jiao, Diarong Chen & Yong Hu, Mater Res Bull, 37 (2002) 1583.
24. Properties and applications of perovskite-type oxides, edited by L. G. Tejuca and J. L. G. Fierro (Marcel Dekker Inc., New York, 1992)],[A. S. Bhalla, R. Guo, and R. Roy, Mat. Res. Innovative. 4, 3 (2000).
25. U. Muller. Anorganische Strukturchemie, in: C. Elschenbroich, F. Hensel, H. Hopf (Eds.), Teubner Studienbucher Chemie. Teubner, Stuttgart, 3rd edition, 1996.
26. J.B Goodenough. Localized to Itinerant Electronic Transition in Perovskite Oxides, in: D.M.P Mingos, Structure and Bonding. Springer, Berlin, 1st edition, 2000.
27. M. A. Pena, J. L. G. Fierro, Chem. Rev. (2001) 1981.
28. A.I. Lebedev, "Ferroelectric properties of RbNbO3 and RbTaO3", Physics Department, Moscow State University, Moscow, 119991 Russia (Dated: January 6, 2015).
29. Roman V. Shpanchenko, "Synthesis, Structure, and Properties of New Perovskite PbVO3", Department of Chemistry, Moscow State University, 119992 Moscow, Russia, 2004.
30. C. Carrétéro, "Hétérostructures d'oxydes de structure pérovskite : Propriétés structurales et éléctroniques de l'interface LaAlO3 / SrTiO3", Thèse doctorat, Université Pierre et Marie Curie, 2010.
31. F. Kubel and H. Schmid, "Structure of a ferroelectric and ferroelastic monodomain crystal of the perovskite BiFeO3", Acta Crystallogr. B, vol. 46, no. 6, pp. 698–702, Dec. 1990.
32. B. REUTER ET M. WOLLNIK, Naturwiss. 17, 569 (1963).
33. J. B. GOODENOUGH, J. Appl. Phys. 37, 1415 (1966).
34. A.I. Lebedevv, "Ferroelectric properties of RbNbO3 and RbTaO3", Physics Department, Moscow State University, Moscow, 119991 Russia (Dated: January 6, 2015).
35. Rune Søndenå, P. Ravindran, and Svein Stølen, "Electronic structure and magnetic properties of cubic and hexagonal SrMnO3", Department of Chemistry and Centre for Materials Science and Nanotechnology, the University of Oslo, Postbox 1033 Blindern, N-0315 Oslo, Norway, 2006.
36. Website: http://www.Empa-perovskite.com, Materials Science &Technology.
37. Hiroshi Mizoguchi, Patrick M. Woodward, Song-Ho Byeon, and John B. Parise, "Polymorphism in NaSbO3: Structure and Bonding in Metal Oxides", Contribution from the Department of Chemistry, Ohio State University, Columbus, Ohio 43210-1185, Department of Geosciences and Mineral Physics.
38. Bobeck, A., Fischer, R., Perneski, A., Remeika, J., & Van Uitert, L. (1969). Application of orthoferrites to domain-wall devices. *IEEE Transactions on Magnetics*, *5*(3), 544-553.
39. Demokritov, S. O., Kirilyuk, A. I., Kreines, N. M., Kudinov, V. I., Smirnov, V. B., & Chetkin, M. V. (1991). Interaction of the moving domain wall with phonons. *Journal of magnetism and magnetic materials*, *102*(3), 339-353.
40. Didosyan, Y. S., Hauser, H., Reider, G. A., & Toriser, W. (2004). Fast latching type optical switch. *Journal of applied physics*, *95*(11), 7339-7341.
41. Tien N.A., Almjasheva O.V., Mittoval.Ya.,etal. Synthesis and magnetic properties of YFeO3 nanocrystals. Inorg. Mater., 2009, 45 (11), P.1304–1308.

42. PopkovV.I.,AlmjashevaO.V.,Schmidt M.P.,etal. Formation mechanism of nanocrystalline yttrium orthoferrite under heat treatment of the coprecipitated hydroxides. Russ. J.Gen.Chem., 2015, 85 (6), P.1370–1375.

43. WuL., YuJ. C., Zhang L., et al. Selective self-propagating combustion synthesis of hexagonal and orthorhombic nanocrystalline yttrium iron oxide. J. SolidStateChem., 2004, 177 (10), P.3666–3674.

44. Popkov V.I., Almjasheva O.V. Yttrium Orthoferrite YFeO3 nanopowders formation under glycine nitrate combustion conditions. Russ. J.Appl.Chem., 2014, 87 (2), P.167–171.

45. Popkov V.I., Almjasheva O.V., Schmidt M.P., etal. Features of Nanosized YFeO3 Formation under Heat Treatment of Glycine Nitrate Combustion Products. Russ. J.Inorg.Chem., 2015, 60 (10), P.1193–1198.

46. Ji, L., Jiang, G., Wu, D., & Chen, J. (2020). Study on the influence of ion doping on the crystal structure and magnetic properties of YFeO3. *Materials Research Express*, *7*(6), 066103.

47. Nagrarw, B, S., Kekade, S. S., Thombare, B., Reddy, R.V., & Patil, S. I. (2018). Hyperfime interation, Raman and magnetic study of $YFeO_3$ nanocrystals. Solid State Communicatios, 280, 32-38.

48. Rosales-González, O., Sánchez-De Jesús, F., Cortés-Escobedo, C. A., & Bolarín-Miró, A. M. (2018). Crystal structure and multiferroic behavior of perovskite YFeO3. Ceramics International, 44(13), 15298-15303.

49. Lü, X., Xie, J., Shu, H., Liu, J., Yin, C., & Lin, J. (2007). Microwave-assisted synthesis of nanocrystalline YFeO3 and study of its photoactivity. Materials Science and Engineering: B, 138(3), 289-292.

50. Popkov, V. I., Almjasheva, O. V., Nevedomskiy, V. N., Panchuk, V. V., Semenov, V. G., & Gusarov, V. V. (2018). Effect of spatial constraints on the phase evolution of YFeO3-based nanopowders under heat treatment of glycine-nitrate combustion products. Ceramics International, 44(17), 20906-20912.

51. Asif, M., Khan, M. A., Atiq, S., Alshahrani, T., Mahmood, Q., Kattan, N. A., & Manzoor, A. (2021). Evolution of structure and improvement in dielectric properties of praseodymium substituted YFeO3 nanomaterials synthesized via a sol-gel auto-combustion method. Ceramics International, 47(5), 6663-6674.

52. Tang, P., Chen, H., Cao, F., & Pan, G. (2011). Magnetically recoverable and visible-light-driven nanocrystalline YFeO 3 photocatalysts. Catalysis Science & Technology, 1(7), 1145-1148.

53. Popkov, V. I., & Almjasheva, O. V. (2014). Formation mechanism of YFeO 3 nanoparticles under the hydrothermal conditions. *Наносистемы: физика, химия, математика*, *5*(5), 703-708.

Chapter 2: Synthesis and characterization methods

A.2.1 Synthesis methods:

A.2.1. a Comparison in Methods of preparation:

The methods used for oxides preparation were classified according to their types and the most common pros on cons of their properties, in order to choose the suitable preparation method for our Spinel and Perovskite oxides [1], the preparation methods were listed in the following points:

- Wet chemical synthesis includes coprecipitation, sol-gel, microemulsion, reverse micelle method, microwave-assisted, hydrothermal, solvothermal, sonochemical, and thermal decomposition are well known with their simplicity, high yield, crystallinity, and purity, also environment-friendly. However, some methods need expensive fuels, the products agglomerate easily, the reactions need large energy with necessity of controlling the conditions to obtain the desired products [2-5].
- Dry chemical synthesis (combustion and solid-state) is suitable type of preparation method for ferrite oxides due to the multiple advantages and lack of disadvantages, because these methods have fast reactions with low equipment that can lead to high yield with obtaining the desired products easily [5].
- Physical methods (Laser-induced pyrolysis and Laser pyrolysis) are considered to be the highest costly equipment even though it can produce very fine particle size composition [2, 4, 5].
- Biological/Biosynthesis methods (Fungi-based, Algae-based, Bacteria-based and plant-based) are the ecofriendly and non-hazardous alternatives to physical and chemical methods giving “homogenous distribution of crystalline nanomaterials” at cost-effectiveness and simple process but the products are unpurified nanoparticles with poor reproducibility and hard to control their sizes and properties [2, 4].

A.2.1.b Chosen synthesis method: Auto-combustion process:

The auto-combustion process of xerogel as an exothermic reaction of anionic redox and self-sustaining thermally-induced, it results from an aqueous solution consisting of the required metal salts “oxidizer” and organic complexant “reductant” [6]. The combustion process of reactant combinations is represented in Fig. A.2.1 [7]. Complexant and salt proportions are typically estimated using the valences of the reactive components in order to achieve an oxidizer/reductant ratio of 1 [8]. Because they are a water-soluble low temperature NO^{-3} oxidant source for synthesis, nitrate salts are preferred as precursors [9].

Metal nitrates and complexants are sometimes mixed immediately by vigorous stirring and heating without the use of water. Metal nitrates are hygroscopic, which means they rapidly absorb moisture and turn into slurry. The flash-combustion method refers to this type of sol-gel auto-combustion [10, 11].

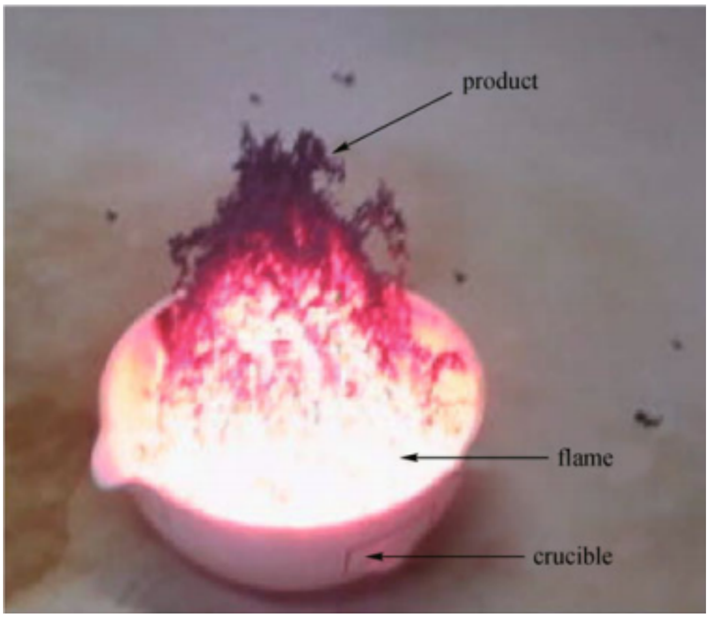

Fig. A.2.1 Combustion reaction of reactant mixture [7].

Rapid analysis of a huge volume of gases, along with loss during the xerogel combustion, resultls in the production of ferrite nanopowders. Agglomeration is limited by the development of gases [12, 13].

The heat released by the exothermic process is undoubtedly responsible for the direct growth of crystalline ferrite from xerogel [14]. During combustion, the flame temperature during can range from 600°C to 1350°C. The flow chart of the processing steps is illustrated in Fig. A.5 [15].

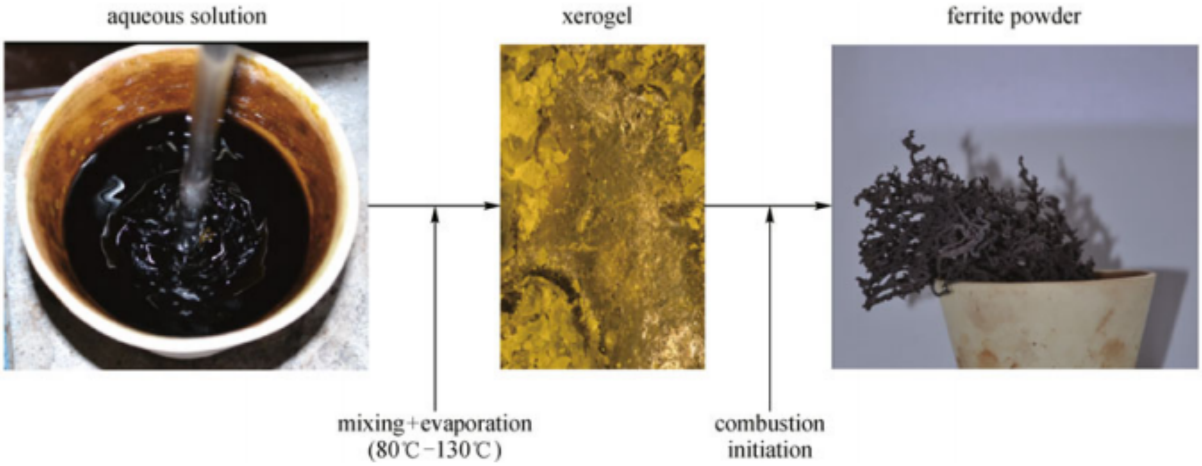

Fig. A.2.2 Flow chart of processing steps [15].

Some of the advantages of sol-gel auto-combustion consist of "high product purity and crystallinity; fine particle size and narrow particle size distributions; easy control of stoichiometry; dopants can be easily incorporated into the final product; simple equipment and preparation process; low processing time; low external energy consumption (process initiates at low temperatures) and multiple steps are not required" [16, 17].

A.2.2. Characterization methods

To investigate and ensure the formation of the desired materials that we synthesized; we need to check their crystallinity by X-ray diffraction (XRD), the morphology of their crystals by Scanning Electronic Microscopy (SEM), also we can study the vibrations in the molecules by identifying their bonds, their intensities and shifts by Fourier Transformed Infrared Spectroscopy (FTIR), and Raman spectroscopy [18-20]. Moreover, to measure the mass changes in function of temperature/time we can use the Thermogravimetric analysis (TG) [21].

References

1. Hammouche, J., Ramachandran, K., Daoudi, K., & Gaidi, M. (2023). Fabrication of magnetic nanosystems for antimicrobial coatings. In *Antimicrobial Nanosystems* (pp. 327-351). Elsevier.
2. Abbas, H. S., & Krishnan, A. (2020). Magnetic nanosystems as a therapeutic tool to combat pathogenic fungi. Advanced Pharmaceutical Bulletin, 10(4), 512.
3. Dippong, T., Levei, E. A., & Cadar, O. (2021). Formation, Structure, and Magnetic Properties of MFe2O4@ SiO2 (M= Co, Mn, Zn, Ni, Cu) Nanocomposites. Materials 2021, 14, 1139.
4. Mihai, A. D., Chircov, C., Grumezescu, A. M., & Holban, A. M. (2020). Magnetite Nanoparticles and Essential Oils Systems for Advanced Antibacterial Therapies. International Journal of Molecular Sciences, 21(19), 7355.
5. Dippong, T., Levei, E. A., & Cadar, O. (2021). Recent Advances in Synthesis and Applications of MFe2O4 (M= Co, Cu, Mn, Ni, Zn) Nanoparticles. Nanomaterials, 11(6), 1560.
6. Airimioaei M, Ciomaga C E, Apostolescu N, et al. Synthesis and functional properties of the Ni1–xMnxFe2O4 ferrites. Journal of Alloys and Compounds, 2011, 509(31): 8065–8072
7. Hwang C-C, Tsai J-S, Huang T-H, et al. Combustion synthesis of Ni–Zn ferrite powder influence oxygen balance value. Journal of Solid State Chemistry, 2005, 178(1): 382–389
8. Costa A C F M, Morelli M R, Kiminami R H G A. Combustion synthesis: Effect of urea on the reaction and characteristics of Ni– Zn ferrite powders. Journal of Materials Synthesis and Processing, 2001, 9(6): 347–352.
9. Selvan R K, Augustin C O, Berchmans L J, et al. Combustion synthesis of CuFe2O4. Materials Research Bulletin, 2003, 38(1): 41–54.
10. Mangalaraja R V, Ananthakumar S, Manohar P, et al. Initial permeability studies of Ni–Zn ferrites prepared by flash combustion technique. Materials Science and Engineering A, 2003, 355 (1–2): 320–324
11. Mangalaraja R V, Ananthakmar S, Manohar P, et al. Characterization of Mn0.8Zn0.2Fe2O4 synthesized by flash combustion technique. Materials Science and Engineering A, 2004, 367(1–2): 301–305.
12. Sertkol M, Kōseoglu Y, Baykal A, et al. Synthesis and magnetic characterization of Zn0.7Ni0.3Fe2O4 nanoparticles via microwave-assisted combustion route. Journal of Magnetism and Magnetic Materials, 2010, 322(7): 866–871
13. Yu L, Cao S, Liu Y, et al. Thermal and structural analysis on the nanocrystalline NiCuZn ferrite synthesis in different atmospheres. Journal of Magnetism and Magnetic Materials, 2006, 301(1): 100–106.
14. Wu K H, Ting T H, Li M C, et al. Sol–gel auto-combustion synthesis of SiO2-doped NiZn ferrite by using various fuels. Journal of Magnetism and Magnetic Materials, 2006, 298(1): 25–32
15. Hwang C-C, Tsai J-S, Huang T-H. Combustion synthesis of Ni–Zn ferrite by using glycine and metal nitrates investigations of precursor homogeneity, product reproducibility, and reaction mechanism. Materials Chemistry and Physics, 2005, 93(2–3): 330–336.
16. Costa A C F M, Morelli M R, Kiminami R H G A. Microstructure and magnetic properties of Ni1–xZnxFe2O4 synthesized by combustion reaction. Journal of Materials Science, 2007, 42(3): 779–783
17. Mukasyan A S, Epstein P, Dinka P. Solution combustion synthesis of nanomaterials. Proceedings of the Combustion Institute, 2007, 31(2): 1789–1795.

18. Ravi Sharma et al, X-ray diffraction: a powerful method of characterizing nanomaterials, Recent Research in Science and Technology 2012, 4(8): 77-79.
19. Chalmers JM, Edwards HGM, Hargreaves MD. Infrared and Raman spectroscopy in forensic science. 1st ed. United Kingdom: John Wiley & Sons Ltd.; 2012.
20. Egerton, R. F. (2016). An introduction to microscopy. In Physical Principles of Electron Microscopy (pp. 1-26). Springer, Cham.
21. Brown, M. E. (2001). Introduction to thermal analysis: techniques and applications (Vol. 1). Springer Science & Business Media.

Chapter 3: Application for water treatment: Photocatalytic activity

It was mentioned in the book of “IUPAC Gold“ that photocatalysis refers to the “change in the rate of a chemical reaction or its initiation under the action of ultraviolet, visible or infrared radiation in the presence of a substance—the photocatalyst—that absorbs light and is involved in the chemical transformation of the reaction partners.” Also, a photocatalyst is described as a “catalyst capable of producing chemical transformations of the reaction partners upon absorption of light. The photocatalyst’s excited state frequently interacts with the reaction partners, creating reaction intermediates and regenerates itself after each cycle of such interactions” [1].

A.3.1. The fundamentals of photocatalysis

Over the last three decades, there has been a considerable increase of researches on photocatalysis on semiconductor surfaces. This is due to the level of similarity with photosynthesis, the most essential natural chemical activity. Photosynthesis is the conversion of H_2O and CO_2 to O_2 and $C_x(H_2O)_y$ by using visible sun light. The fundamental processes in that fascinating heterogenous photocatalytic proves are photochemical charge production, charge trapping, interfacial electron exchange, and C–C coupling. Molecular systems may reproduce the first two stages, but not the latter two steps, which include the chemical synthesis phase. After irradiating a semiconductor powder solution in the presence of electrons as donors and the substrates as acceptors, simple C–C, H–H, and C–N couplings become conceivable [2]. Charges generated by light are locked at the surface and react with the substrates in coordinated interfacial reduction and oxidation processes. The main products are often short-lived radicals that are transformed to final products by the creation of selected chemical bonds. As a consequence, the semiconductor can do at least two activities. It promotes appropriate substrate assembly by adsorption at the surface–solvent layer and catalyses photoinduced interfacial electron transport to and from substrates, which is usually combined with proton transfer. Water splitting, molecular nitrogen fixation, and alkane functionalization are examples of such heterogeneous systems' high reactivity. While much emphasis has been placed on water splitting and rigorous aerobic pollution degradation have received a lot of attention, barely any kind of study has concentrated on the aspects of synthesis [3].

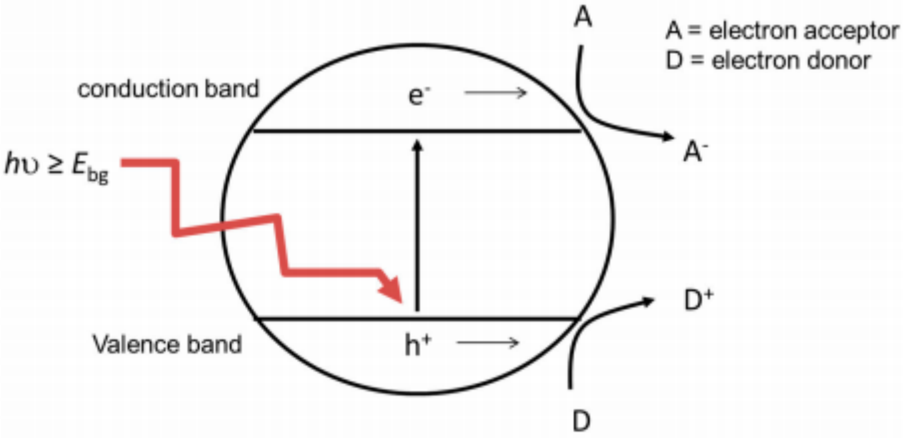

Figure A.3.1 Representative graph of heterogeneous photocatalysis mechanism.

Absorption of electromagnetic radiation on the valence band (VB) with energy equals to or higher than the bandgap energy (Eg) excites the semiconductor. This causes an electron to be promoted to the conduction band (CB), and creates on the VB a hole charged positively. The pairs of "electron-hole" can recombine with the re-emitted energy, either as heat or light, or the charge transporters can move to the material surface. The electron in the CB can be transferred to an electron acceptor with a higher "positive electrochemical reduction potential" (PERP) than the electron in the CB edge potential. The hole in the VB can receive electrons from donor species that have a lower PERP than the VB edge. These processes reduce the acceptor species and oxidize the donor species, with these two reactions being conducted by the potential difference promoted by the electromagnetic radiation absorption. This potential difference produced is nearly to the semiconductor's bandgap energy [4].

Photocatalysis processes are thermodynamically downhill (−ve ΔG), while photosynthesis reactions are thermodynamically uphill (+ve ΔG). However, the word "photocatalytic" is commonly used describe uphill processes, such as "photocatalytic" water splitting. We are especially interested in surface redox processes that result in the formation of reactive oxygen species (ROS). Figure A.3.2 represents a general approach for the formation of reactive oxygen species in which oxygen functions as as an electron acceptor and water or hydroxyl ions functions as an electron donor. Titanium dioxide (TiO_2) is the semiconductor in this scenario due to the potentials of the band edge must be in the appropriate spot to initiate the reactions. In the infrared region, other semiconductor materials may be utilized. The hole in VB may have an electrochemical potential reduction that is charged positively enough to oxidize H_2O and produce $HO^{\cdot}$, whereas the CB should be charged negatively enough to reduce O_2 and produce the anion of superoxide radical, and then peroxide and hydroxyl radical via subsequent electron transfer. Overall, the photocatalytic process may create a combination of ROS in the presence of O_2 and H_2O, that can inactivate bacteria or breakdown organic chemical pollutants [5, 6].

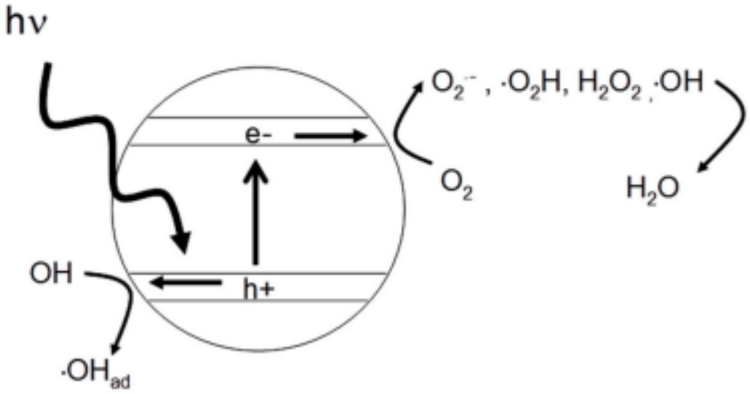

Figure A.3.2 Scheme of photocatalytic mechanism on a titanium dioxide particle leading to the production of reactive oxygen species.

References

1. IUPAC. Compendium of Chemical Terminology. In The Gold Book, 2nd ed.; McNaught, A.D., Wilkinson, A., Eds.; Blackwell Scientific Publications: Oxford, UK, 1997.

2. Habisreutinger, S. N., Schmidt-Mende, L., & Stolarczyk, J. K. (2013). Photocatalytic reduction of CO2 on TiO2 and other semiconductors. Angewandte Chemie International Edition, 52(29), 7372-7408.

3. Kisch, H. (2015). Semiconductor photocatalysis: principles and applications. John Wiley & Sons.

4. Mills, A.; Le Hunte, S. An overview of semiconductor photocatalysis. J. Photochem. Photobiol. A 1997, 108, 1–35.

5. Malato, S.; Fernandez-Ibanez, P.; Maldonado, M.I.; Blanco, J.; Gernjak, W. Decontamination and disinfection of water by solar photocatalysis: Recent overview and trends. Catal. Today 2009, 147, 1–59.

6. N. Barsan et al, Metal oxide-based gas sensor research: How to?, Elsevier, 2006.

Part B: Experimental and application

Disclaimer:

-The following part is our work so no need to check the percentage of plagiarism. Also, the journal allowed us to add this work to the thesis.

-The samples of Ni-doped ZFO with 0%, 5%, 15%, 30%, and 40% are published and can be cited by: Hammouche, J., Gaidi, M., Columbus, S., & Omari, M. (2021). Enhanced photocatalytic performance of zinc ferrite nanocomposites for degrading methylene blue: effect of nickel doping concentration. *Journal of Inorganic and Organometallic Polymers and Materials*, *31*, 3496-3504.

-We are going to publish the rest of Ni-doping percentages soon.

-We do not allow anyone to copy or to share the non-published percentages until it will be published.

تنويه:

- هذا الجزء يعتبر عملنا الخاص لذا لا حاجة لقياس نسبة الاقتباس. كذلك المجلة سمحت لنا بإضافته إلى المذكرة.

- عينات النيكل المضافة إلى أكسيد حديد الزنك ذات النسب ٠٪، ٥٪، ١٥٪، و ٤٠٪ قد تم نشرها و يمكن تهميشها كمرجع ب: Hammouche, J., Gaidi, M., Columbus, S., & Omari, M. (2021). Enhanced photocatalytic performance of zinc ferrite nanocomposites for degrading methylene blue: effect of nickel doping concentration. *Journal of Inorganic and Organometallic Polymers and Materials*, *31*, 3496-3504.

- سنقوم بنشر بقية نسب إضافة النيكل قريبا.

- لا نسمح لأي أحد بنسخ أو مشاركة نسب الإضافة غير المنشورة إلا بعد أن يتم نشرها.

Chapter 1: Preparation, Characterization methods and photocatalytic activity for $ZnFe_{2-x}Ni_xO_4$

The ZFO samples were synthesized by auto-combustion method then characterized by: X-Ray diffractometer (D8 advanced Bruker), Raman spectroscopy (RENISHAW) with laser edge 785 nm, FTIR (JASCO FT/IR-6300), Field Emission SEM (Thermo scientific Apreo C). The Ni content in the $ZnFe_{2-x}Ni_xO_4$ prepared samples has been changed from $x = 0.05$ to 0.6.

B.1.1. Preparation of Ni-doped ZFO:

- Chemicals: Base materials such as zinc nitrate ($Zn(NO_3)_2.6H_2O$), ferric nitrate ($Fe(NO_3)_3.\ 9H_2O$), nickel nitrate ($Ni(NO_3)_2.6H_2O$), glycine ($C_2H_5NO_2$) from Sigma Aldrich, USA and methylene blue from IBA scientific, IA were used for the present study [1].

- Process of preparation:

ZFO samples were prepared by dissolving and mixing the nitrates of Zinc, Iron and nickel as precursors and glycine as fuel then stirring and heating the solution at 80°C until the formation of homogenous gel and its combustion; according to the work of (Hwang, Tsai et al. 2005). the flame temperature during combustion can be from 600 to 1350 °C. After burning in the air and grinding, the burned gel turned to powder. All samples have then been annealed at 1000 °C under air as shown in the following chart representing the steps of the synthesis:

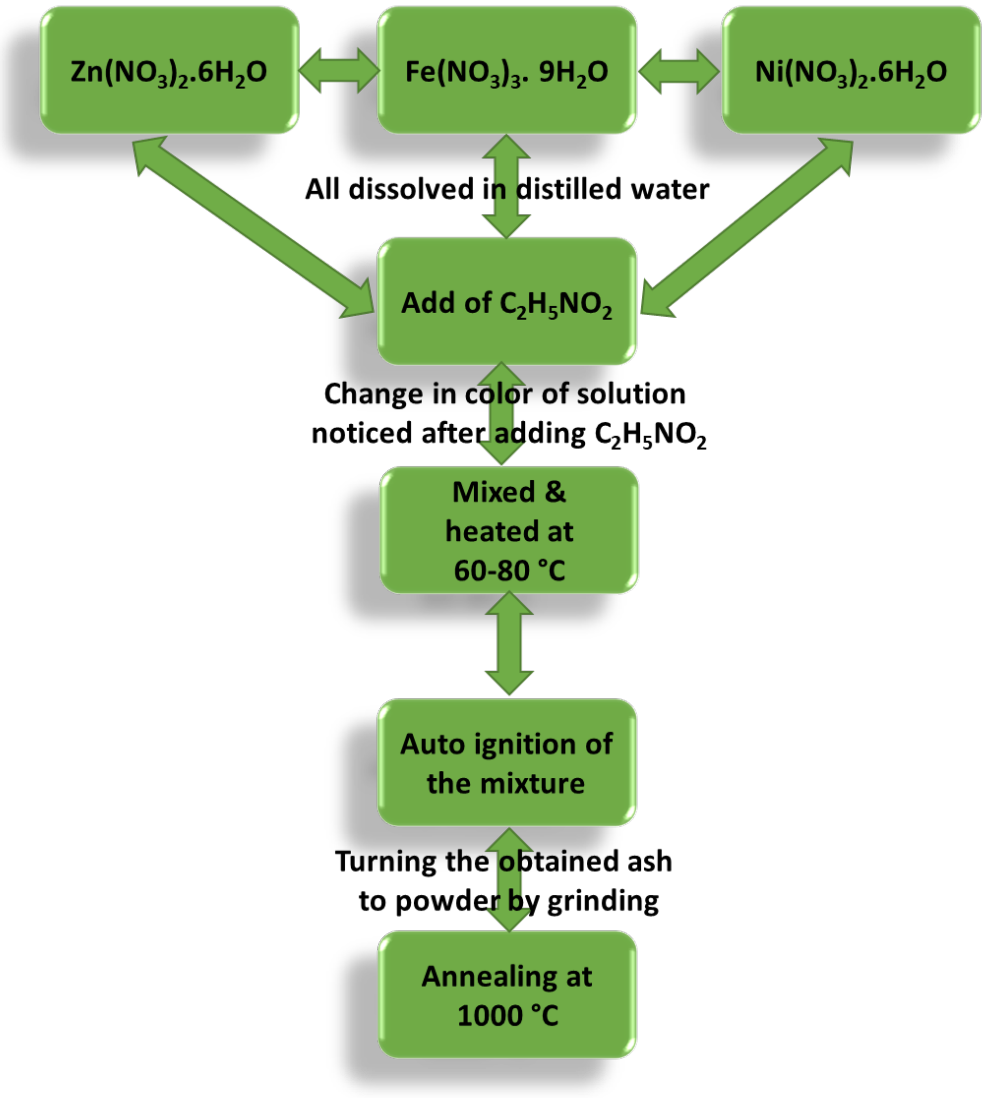

Fig. B.1.1: Chart of ZFO preparation steps by the auto-combustion method.

- Photocatalysis application:

The photocatalytic activity of as-prepared samples was evaluated using a photochemical reactor (Techinstro, India) equipped with a 450W ultraviolet (UV) lamp. For this, 300 ml aqueous solution of methylene blue (0.02×10^{-3} mol/L) was taken in the reaction vessel followed by the addition of 0.1 g of ZFO doped by Ni (x = 0, 0.05, 0.15, 0.3, and 0.4) Adsorption-desorption equilibrium of dye on the photocatalyst surface was ensured by magnetic stirring in dark for 20 min. The reaction medium is then subjected to UV light and the temperature was kept steady during the reaction using an external water circulatory chiller unit. The decrease in absorption values of MB solutions was continuously monitored at each 20 min time interval using a UV-visible spectrophotometer [3]. The degradation efficiency is calculated using the following equation:

$$\text{Degradation of dye (\%)} = [(C_0 - C_t) / C_0] \times 100\% \qquad (1)$$

$$= [(A_0 - A_t) / A_0] \times 100\% \qquad (2)$$

Where C_0 and C_t are the initial and the final concentrations, respectively; A_0 and A_t are the corresponding absorbance values of MB, which were measured at the highest absorbance peak of MB of 665nm.

B.1.2. Results and discussion

B.1.2.a Structural characterization

ZFO nanocomposites were successfully synthesized by auto-combustion method by varying the Ni content from 5 to 60 % of $ZnFe_{2-x}Ni_xO_4$ (x = 0, 0.05, 0.1, 0.15, 0.2, 0.3, 0.4, 0.5 & 0.6). The diffractograms of the synthesized samples were annealed at 1000 °C (Fig. B.2a). The diffractograms of the synthesized samples $ZnFe_{2-x}Ni_xO_4$ (x = 0, 0.05, 0.1, 0.15, 0.2, 0.3, 0.4, 0.5 & 0.6) annealed at 1000 °C shown in figure 1 with their crystal sizes; were analyzed by X’Pert high score software to check their structure allowed us according to find that the diffraction peaks of sample x = 0 & 0.1 are in a good agreement with the ASTM card no. (01-073-1963) of pure Zinc Ferrite cubic phase with space group Fd3m without any extra peaks of other oxides were produced, where x = 0.05, 0.15, 0.2, 0.3, 0.4, 0.5 & 0.6 their diffraction peaks are in good agreement with the ASTM card no. (01-073-1963) of pure Zinc Ferrite cubic phase with space group Fd3m and extra peaks with ASTM card no. (00-001-1136) of ZnO hexagonal wurtzite nanoparticles only [4, 5].

The average crystallite size of zinc ferrites compositions was calculated from the XRD spectra using the Debye-Scherrer formula [6, 7]

$$D = \frac{0.9\lambda}{\beta\cos\theta} \qquad (3)$$

where D is the crystalline size, λ denotes the wavelength of Cu-Kα X-ray radiation, β is the full width at half maximum of XRD peaks and θ is Bragg's angle. The variation of the crystal size of ZFO compositions was plotted as a function of Ni dopant concentration as shown in Fig. 1b. It can be seen that subsequent changes in Ni content impose a slight variation of crystal sizes from 55 to 88 nm. While lower and higher doping concentrations (10%, 20%, 50% & 60 % respectively) resulted in slightly higher crystal size, the lowest crystal size was obtained for moderate Ni doping levels of 0%, 5%, 15%, 30 % & 40%.

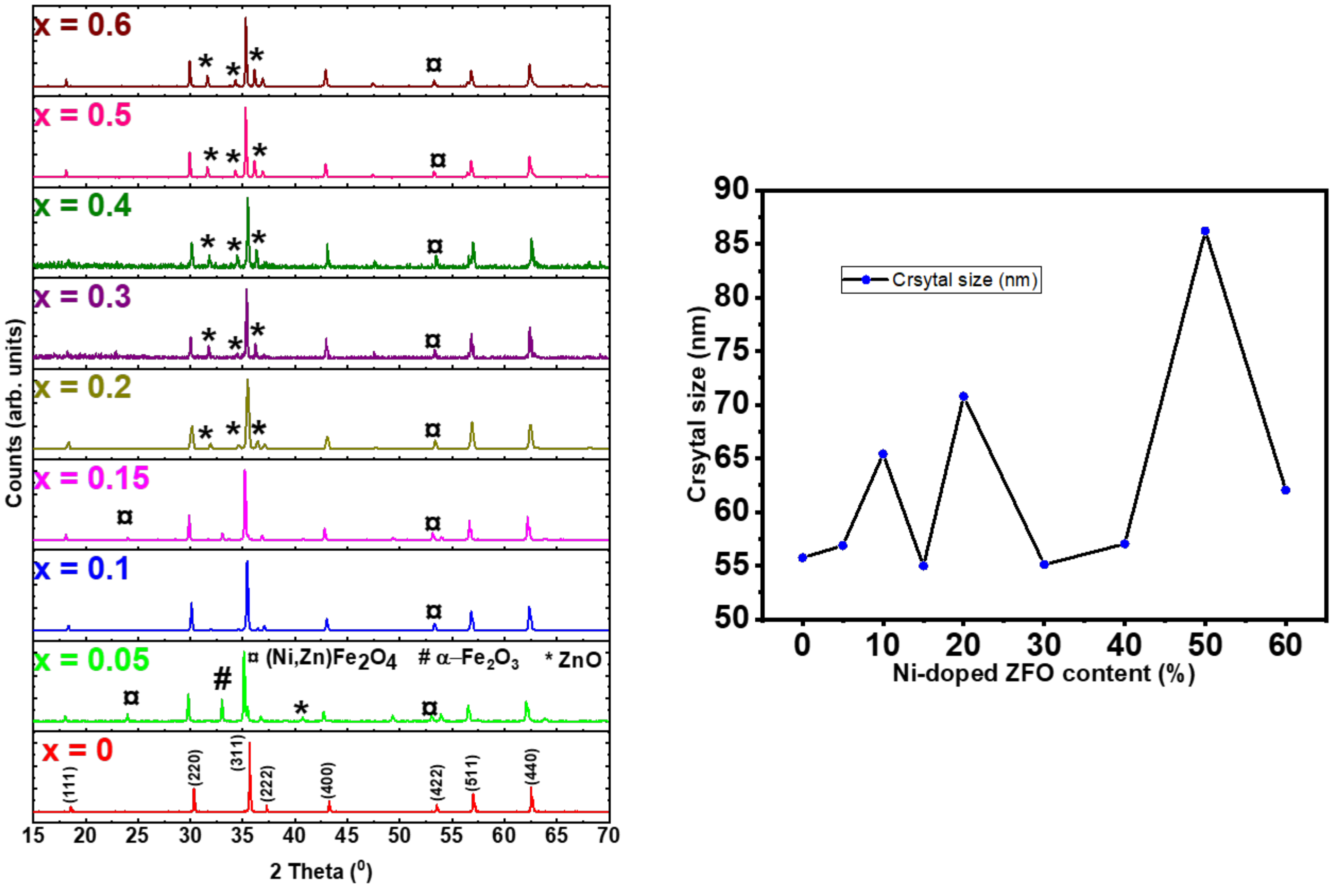

Fig. B.1.2 On left: XRD pattern of $ZnFe_{2-x}Ni_xO_4$ powder as a function of Ni doping (x=0, 0.05, 0.1, 0.15, 0.3, 0.4, 0.5 and 0.6) after annealing at 1000°C under air, and on right: Plot of crystal size versus Ni dopant concentration.

The characteristic Raman spectra of synthesized ZFO samples were represented in Fig. B.1.2 It was reported that the positions of the peaks, Raman lines features, widths, energies, shape and intensities get affected by the substitution leading to the changes in the lattice parameters and the cations positions in the lattice. The Raman shifts shows 5 modes ($A_{1g} + E_g + 3F_{2g}$) as normal spinel-type for samples with x = 0, 0.05, 0.1, 0.15 & 0.2 and inverse spinel-type for x = 0.3, 0.4, 0.5 & 0.6 ones due to A_{1g} mode represented as doublet peaks [6, 8]. It is noticed that Ni dopant percentage is increasingly affected on the spinel structure type by the changes in the cations positions lattice which led to the spinel-type changes from normal to an inverse type.

Tab. B.1.1: Main Raman modes peak energy (cm^{-1}) represented in $ZnFe_{2-x}Ni_xO_4$ annealed at 1000°C.

Ni-doped ZFO content	$F_{2g}(1)$	E_g	$F_{2g}(2)$	$F_{2g}(3)$	$A_{1g}(1)$	Other signals
X = 0	223.2	287.89	348.1	404.4	605.9 (ZnO) 658.32 (FeO)	176, 240.38, 492.5
X = 0.05	180.4	241.57	337.65	490.6	616.86 (ZnO) 704.31 (FeO)	800-noise
X = 0.1	162.1	248.6	343.17	473.4	645.3	119.1, 183.17
X = 0.15	189.02	228.23	328.63	477.25	643.14	800-noise
X = 0.2	127.9	162.3	333.47	475.05	640.86	800-noise
X = 0.3	127.84	189.02	333.33	481.57	647.45 (ZnO) 687.06 (FeO)	233
X = 0.4	127.84	158.43	333.33	473	652.15 (ZnO) 695.7 (FeO)	263.14
X = 0.5	157.9	197.7	329	467.3	658.68 (ZnO) 685.7 (FeO)	127.7
X = 0.6	92.27	162.1	329.2	469.87	651.64 (ZnO) 691.05 (FeO)	800-noise

FTIR spectra of the synthesized ZFO samples were depicted in Fig. B.1.3. Ferrites spinel oxides are reported to consist of two metal-oxygen (M-O) vibrations within the 350-600 cm^{-1} range. The characteristic absorption peaks are observed between 542 and 549 cm^{-1} due to the stretching vibrations of the Fe-O bonds in octahedral positions [7, 9]. Furthermore, the characteristic peaks observed between 401 and 415 cm^{-1} are due to the stretching vibrations of the Zn-O bonds in tetrahedral positions [10, 11]. The peak around 2900 cm^{-1} is not prominent still present in ZFO compositions; which represents C-H stretching vibrations. The absence of a peak around 3000 cm^{-1} indicates the absence of water moieties, mostly due to the annealing process and it was noticed only for 50% and 60%. Further, the peak near 2300 cm^{-1} is mainly due to carbon dioxide molecules that are adsorbed on the substrates. Also, C=C, C-O, Zn-OH and C-OH at 1300 cm^{-1}, 1100 cm^{-1}, 800 cm^{-1}, and 1250 cm^{-1} respectively.

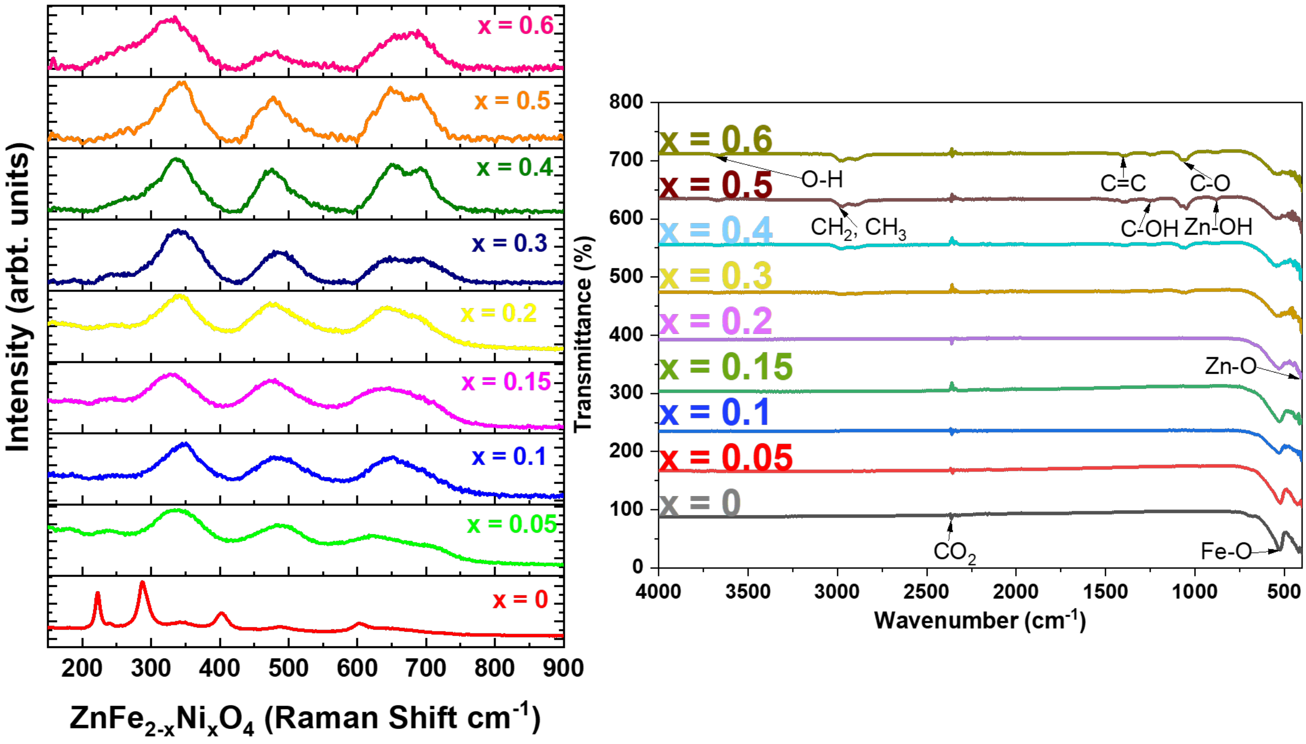

Fig. B.1.3 On left: Effect of Ni content (x = from 0 to 0.6) on the Raman spectra of the $ZnFe_{2-x}Ni_xO_4$ composites annealed at 1000°C under air. Raman spectra acquired using 785 nm laser, 50 mW power and 10 s integration time, and on right: FTIR spectra of $ZnFe_{2-x}Ni_xO_4$ with varying Ni content (x = from 0 to 0.6) after annealing at 1000° C.

B.1.2.b Morphological analysis

The SEM micrographs of ZFO samples showed surface morphology of as-prepared samples (Fig. B.1.4). The grain size was found to be in the range of 103 to 766 nm for different compositions. Moreover, it could be noted that the particle size gets increased on the initial addition of Ni from 5 to 60 %. Some extent of agglomeration has clearly appeared in all compositions which might be attributed due to the exposure to higher temperatures during auto-combustion and annealing processes. The high surface area to volume ratio and inherent magnetic properties of nanoparticles can further facilitate the tendency for agglomeration. Our observation sounds well with previous studies conducted by Naik et al for green synthesis of zinc ferrite nanoparticles using Limonia acidissima juice [12]. Moreover, the elemental analysis showed that as-synthesized zinc ferrites are composed of expected constituent elements such as Zn, Fe, O and Ni [13]. This proved that the auto-combustion process produces pure zinc ferrites without any impurities (Fig. B.1.5).

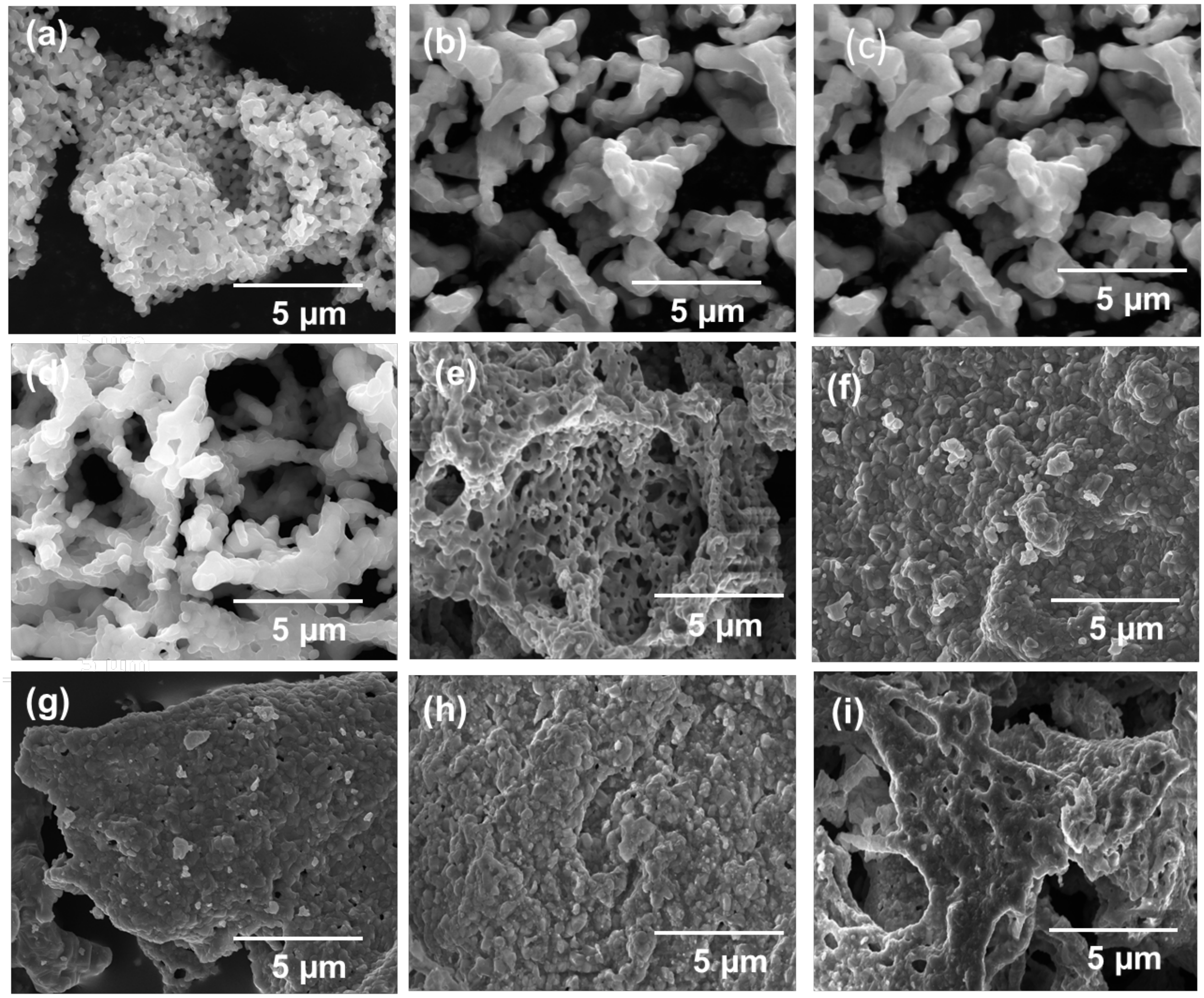

Fig. B.1.4 FESEM images of $ZnFe_{2-x}Ni_xO_4$ samples containing (a) 0, (b) 0.05, (c) 0.1, (d) 0.15, (e) 0.2, (f) 0.3, (g) 0.4, (h) 0.5 and (i) 0.6 % Ni dopant; post annealing at 1000°C.

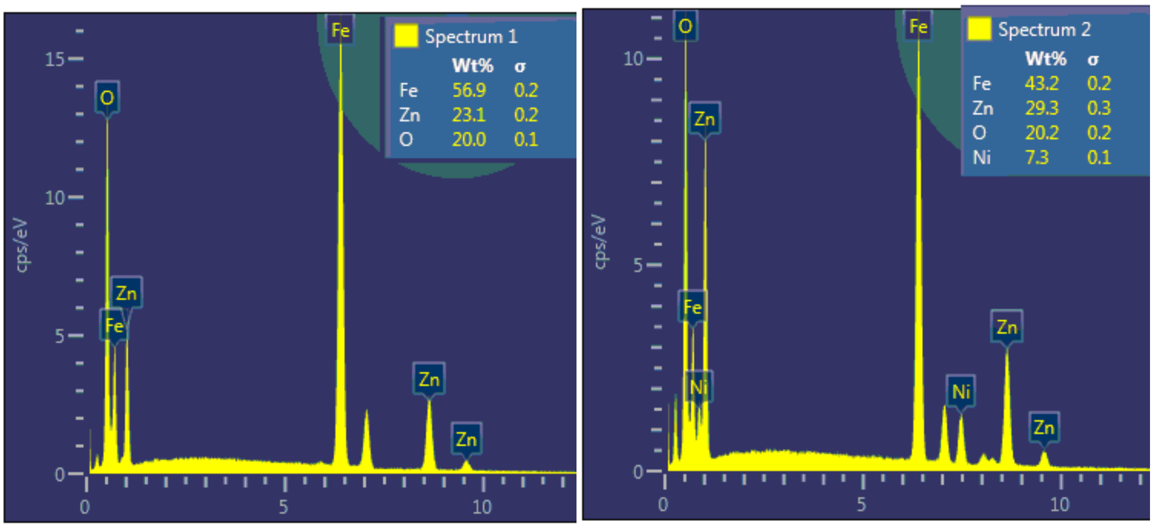

Fig B.1.5. EDX spectra of (a) bare zinc ferrites (b) Ni-Zinc ferrites with 30% Ni loading.

B.1.2.c Photocatalytic activity

The photocatalytic behaviour of as-synthesized ZFO composites was investigated using methylene blue under UV light. The absorbance of MB subsequently decreased with increased during the reaction (Fig. 6a). It could be clearly seen that the photocatalytic performance of ZFO nanocomposites enhanced successively with Ni dopant up to 30 % and thereafter decreases by 40% (Figure 6b & c). After 200 min reaction, the degradation efficiencies of different composites were calculated and correlated with their corresponding crystal size (Fig. 7a). While bare ZFO exhibits ~95 % degradation of MB, zinc ferrite composites with 30 % Ni dopant found to have the highest degradation efficiency of ~98 %. Moreover, the rate constant of the reaction was also calculated for each nanocomposite as given in Fig. 7b. The highest rate constant of 2.38 x 10^{-2} was observed at 30 % Ni content. The photocatalytic efficiency is then strongly correlated to the crystal size of nanocomposites. As the size is decreasing the specific surface area is increasing leading to a more exposed surface for dye adsorption. Besides, the reusability of the synthesized composites was evaluated by subjecting to photocatalysis for three cycles after subsequent washing with deionized water (Fig. 7c). The degradation efficiency of ZFO composites showed more than 85% reproducibility after three cycles. The observed reduction in efficiency might be due to the material loss during washing steps which could be improved by retrieving from the medium using an external magnetic field [1].

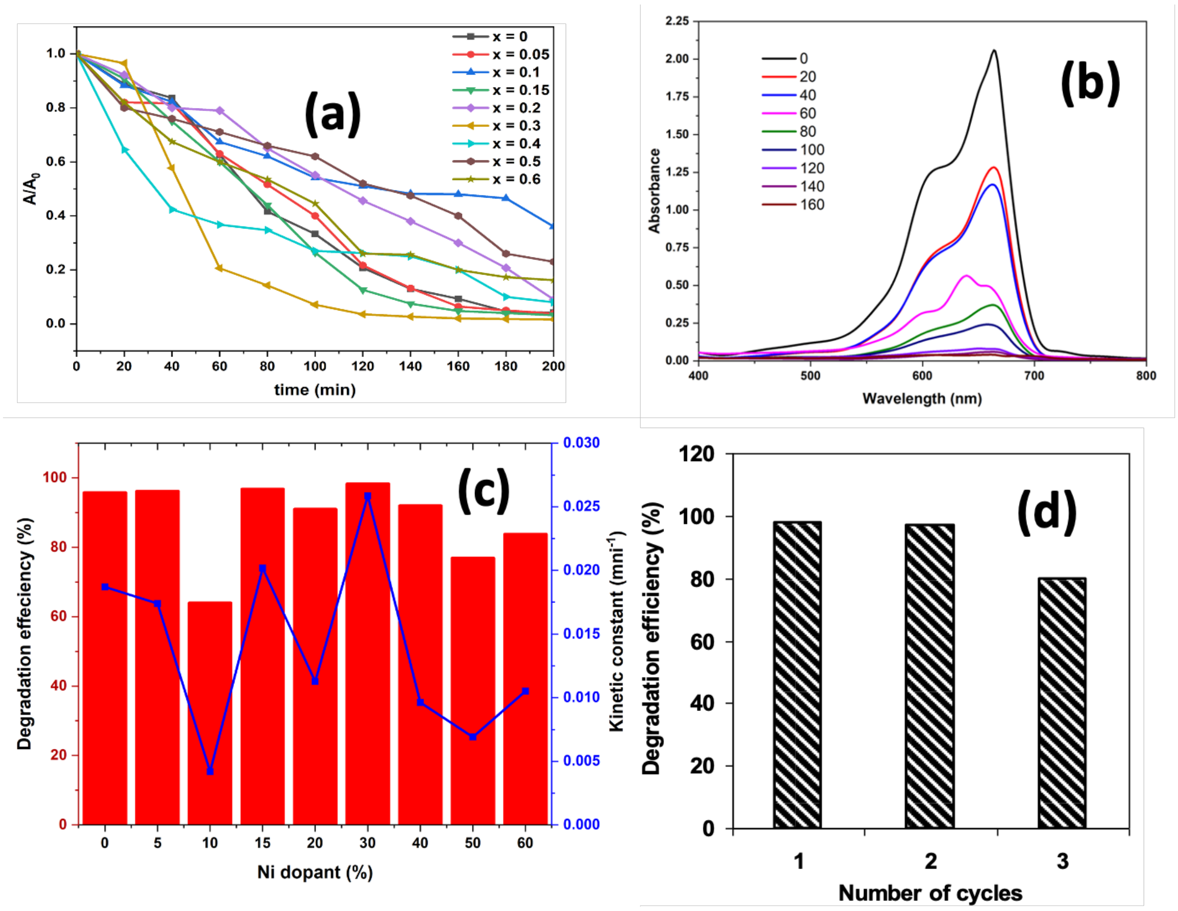

Fig. B.1.6 Effect of Ni doping content on the photocatalysis of methylene blue by zinc ferrite nanocomposites annealed at 1000°C; (a) A plot of absorbance versus irradiation time, (b) Absorbance spectra of MB during photocatalysis, (c) Plot showing the variation of kinetic constant and degradation efficiency with Ni doping of photocatalysis reaction and (d) reusability of synthesized composite Zinc Ferrite Ni-doped 30%.

Fig. B.1.7 demonstrated the feasible photocatalytic mechanism of ZFO nanocomposites. When exposed to UV light, ZFO composites absorb enough energy to excite the electrons from valence band (VB) to conduction band (CB), forming free electrons (e^-) in CB and holes (h^+) in VB [14, 15]. The free electrons may be released into the aqueous solution of dye, which reacts with dissolved oxygen in the medium to form superoxide radicals (O_2^-). These can further attack water molecules or hydroxyl ions to form reactive hydroxide ions ($OH^\cdot$); that have the capacity to attack the dye molecules [16, 17]. Meanwhile, h^+ in the valence band can also promote the formation of $OH^\cdot$ radicals. Consequently, MB can decompose to nontoxic degradation products such as CO_2 and H_2O. The resultant changes in the MB solution were also depicted in the figure.

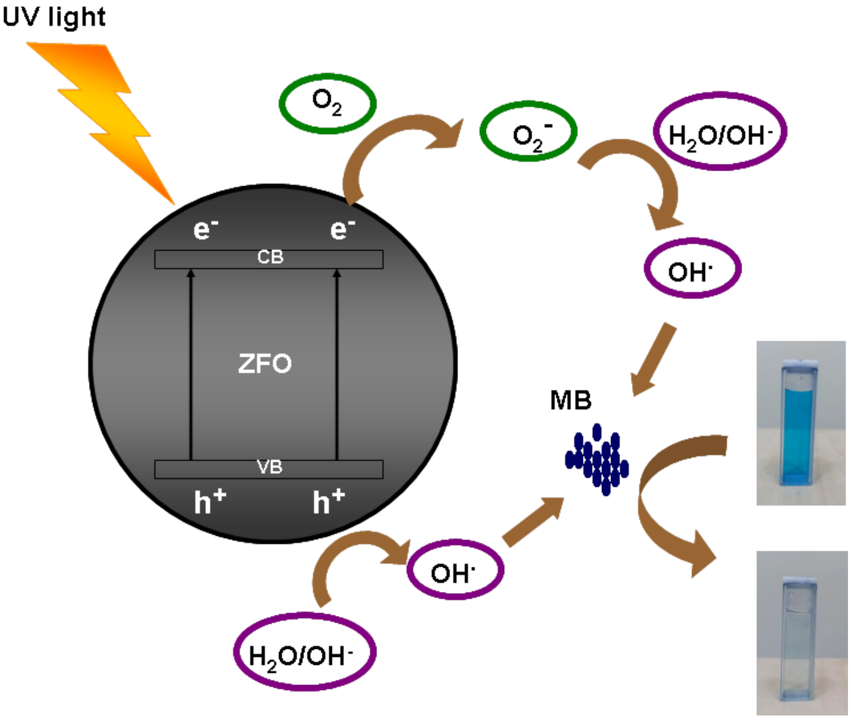

Fig. B.1.7 The proposed mechanism of photocatalysis of MB solutions using ZFO nanocomposites.

We have compared the photocatalytic efficiency obtained for as prepared Ni-doped zinc ferrites with other systems used for methylene blue degradation (Table B.3). A previous investigation by Jadhav *et al* demonstrated the effect of Ni dopant on structural parameters and photocatalytic degradation of Rhodamine B [18]. They found that the photocatalytic effect increases with Ni content while using urea as fuel. In the present study, we have investigated the effect of Ni doping on structural and photocatalytic properties of ZFO nanocomposites by using glycine as a green fuel. We observed that the highest photocatalytic activity of 98% was obtained for the optimum Ni content of 30 %. As auto-combustion process parameters could significantly affect the structure and properties of ZFO nanocomposites, the proper correlation between structural features and photocatalytic performance is highly necessitated in this context.

Table B.1.3: Comparison of photocatalytic activity of currently investigated ZFO composites with previous reports.

Photocatalyst material	Concentration of MB	Irradiation time (min)	Degradation efficiency (%)	Earlier reports
PANI/Zirconium (IV) silicophosphate	1.5 x 10^{-5} M	120	82	Pathania et al. (2014)
Pectin zirconium (IV) selenotungstophosphate	1.5 x 10^{-5} M	180	89	Gupta et al. (2015)
Zinc ferrites	20 ppm	90	94	Padmapriya et al (2016)
Cobalt zinc ferrite	10 mg/L	60	77	Chahar et al. (2021)
Aluminium zinc ferrites	5 ppm	120	55	Mathubala et al. (2016)
Ni dopped Zinc ferrites	2 x 10^{-5} M	180	98	Present work

B.1.3. Conclusions

In summary, ZFO nanocomposites with varying Ni dopant were successfully synthesized using auto-combustion followed by the annealing process. XRD revealed the formation of zinc ferrites crystallites with cubic spinel structure. The morphology of different zinc ferrites was evaluated using SEM. The degradation rate of MB solution increases successively with Ni doping up to 30% and thereafter decreases. With an optimum Ni doping (30%), photocatalytic activity up to 98% was achieved with as-synthesized ZFO nanocomposites, which can perform as an environmentally friendly, easily isolable and recyclable photocatalyst for water treatments.

References

1. *Hammouche, J., Gaidi, M., Columbus, S., & Omari, M. (2021). Enhanced photocatalytic performance of zinc ferrite nanocomposites for degrading methylene blue: effect of nickel doping concentration.* Journal of Inorganic and Organometallic Polymers and Materials, 31, *3496-3504.*
2. Hwang, C.-C., J.-S. Tsai, and T.-H. Huang, Combustion synthesis of Ni–Zn ferrite by using glycine and metal nitrates—investigations of precursor homogeneity, product reproducibility, and reaction mechanism. Materials Chemistry and Physics, 2005. 93(2-3): p. 330-336.
3. Gaidi, M., et al., Enhanced photocatalytic activities of silicon nanowires/graphene oxide nanocomposite: Effect of etching parameters. Journal of Environmental Sciences, 2020. **101**: p. 123-134.
4. Manoharan, C. and S. Dhanapandian, Structural and optical properties of pulse plated cadmium selenide films. Int. J. Recent Sci. Res., 2011. 2: p. 306-308.
5. Guinier, A., Théorie et technique de la radiocristallographie. 1964, Dunod.
6. Meng, W., et al., Photocatalytic activity of highly porous zinc ferrite prepared from a zinc-iron (III)-sulfate layered double hydroxide precursor. Journal of Porous Materials, 2004. 11(2): p. 97-105.
7. Phumying, S., et al., Nanocrystalline spinel ferrite (MFe2O4, M=Ni, Co, Mn, Mg, Zn) powders prepared by a simple aloe vera plant-extracted solution hydrothermal route, Mater. Res. Bull. 2013. 48: p. 2060-2065.
8. Galinetto, P., et al., Raman Spectroscopy in Zinc Ferrites Nanoparticles. Raman Spectroscopy, 2018. 223.
9. Yadav R.S., et al., Structural, magnetic, optical, dielectric, electrical and modulus spectroscopic characteristics of ZnFe2O4 spinel ferrite nanoparticles synthesized via honey-mediated sol-gel combustion method. Journal of Physics and Chemistry of Solids. 2017, 110: p. 87-99.
10. Rezaei, M., et al., Selective and rapid extraction of piroxicam from water and plasma samples using magnetic imprinted polymeric nanosorbent: Synthesis, characterization and application, Colloids and Surfaces A: Physicochemical and Engineering Aspects, 2020. 586: p.124253.
11. Rajabi, H.M., et al, Comparison investigation on photocatalytic activity performance and adsorption efficiency for the removal of cationic dye: Quantum dots vs. magnetic nanoparticles, Journal of Environmental Chemical Engineering, 2016. 4(3): p. 2830-2840.
12. R. Rameshbabu et al., Synthesis and study of structural, mor-phological and magnetic properties of ZnFe2O4 nanoparticles. J. Supercond. Novel Magn. 27(6), 1499–1502 (2013).
13. *Lassoued, A., Lassoued, M. S., Dkhil, B., Ammar, S., & Gadri, A. (2018). Retracted Article: Photocatalytic degradation of methylene blue dye by iron oxide (α-Fe2O3) nanoparticles under visible irradiation. Journal of Materials Science: Materials in Electronics, 29(10), 8142-8152.*
14. *Naik, M. M., Naik, H. B., Nagaraju, G., Vinuth, M., Naika, H. R., & Vinu, K. (2019). Green synthesis of zinc ferrite nanoparticles in Limonia acidissima juice: characterization and their application as photocatalytic and antibacterial activities. Microchemical Journal, 146, 1227-1235.*

15. *Padmapriya, G., Manikandan, A., Krishnasamy, V., Jaganathan, S. K., & Antony, S. A. (2016). Spinel NixZn1− xFe2O4 (0.0≤ x≤ 1.0) nano-photocatalysts: synthesis, characterization, and photocatalytic degradation of methylene blue dye. Journal of Molecular Structure, 1119, 39-47.*
16. *Rajabi, H. R., Karimi, F., Kazemdehdashti, H., & Kavoshi, L. (2018). Fast sonochemically-assisted synthesis of pure and doped zinc sulfide quantum dots and their applicability in organic dye removal from aqueous media. Journal of Photochemistry and Photobiology B: Biology, 181, 98-105.*
17. *Yadav, R. S., Kuřitka, I., Vilcakova, J., Urbánek, P., Machovsky, M., Masař, M., & Holek, M. (2017). Structural, magnetic, optical, dielectric, electrical and modulus spectroscopic characteristics of ZnFe2O4 spinel ferrite nanoparticles synthesized via honey-mediated sol-gel combustion method. Journal of Physics and Chemistry of Solids, 110, 87-99.*
18. *J.S. Jang, S.J. Hong, J.S. Lee, P.H. Borse, O.S. Jung, T.E. Hong, H.G. Kim, Synthesis of zinc ferrite and its photocatalytic appli- cation under visible light. J. Korean Phys. Soc.* ***54****(1), 204–208 (2009).*

Disclaimer:

-The following part is not published yet. We are going to publish it soon after adding electrochemical tests.

-We do not allow anyone to copy or to share this part until it will be published to be referenced.

تنويه:

- الجزء التالي لم يتم نشره بعد. سنقوم بنشره قريبا بعد إضافة التحاليل الكهروكيميائية.

- لا نسمح لأي أحد بنسخ أو مشاركة هذا الجزء إلا بعد أن يتم نشره كي ينسب إلى المرجع.

Chapter 2: Preparation, Characterization methods and photocatalytic activity for $Y_{1-x}Cu_xFeO_3$

The YFO samples were synthesized by auto-combustion method then characterized by: X-Ray diffractometer (D8 advanced Bruker), Raman spectroscopy (RENISHAW) with laser edge 785 nm, FTIR (JASCO FT/IR-6300), Field Emission SEM (Thermo scientific Apreo C). The Cu content in the $Y_{1-x}Cu_xFeO_3$ prepared samples has been changed from x = 0.1 to 0.4.

B.2.1. Preparation of Cu-doped YFO:

- Chemicals: Base materials such as Yttrium nitrate ($Y(NO_3)_2.6H_2O$), ferric nitrate ($Fe(NO_3)_3.\ 9H_2O$), copper nitrate ($Cu(NO_3)_2.6H_2O$), glycine ($C_2H_5NO_2$) from Sigma Aldrich, USA and methylene blue from IBA scientific, IA were used for the present study.

- Process of preparation:

YFO samples were prepared by dissolving and mixing the nitrates of Yttrium, Iron and copper as precursors and glycine as fuel then stirring and heating the solution at 80°C until the formation of homogenous gel and its combustion; according to the work of (Hwang, Tsai et al. 2005). the flame temperature during combustion can be from 600 to 1350 °C. After burning in the air and grinding, the burned gel turned to powder as shown in the following chart representing the steps of the synthesis:

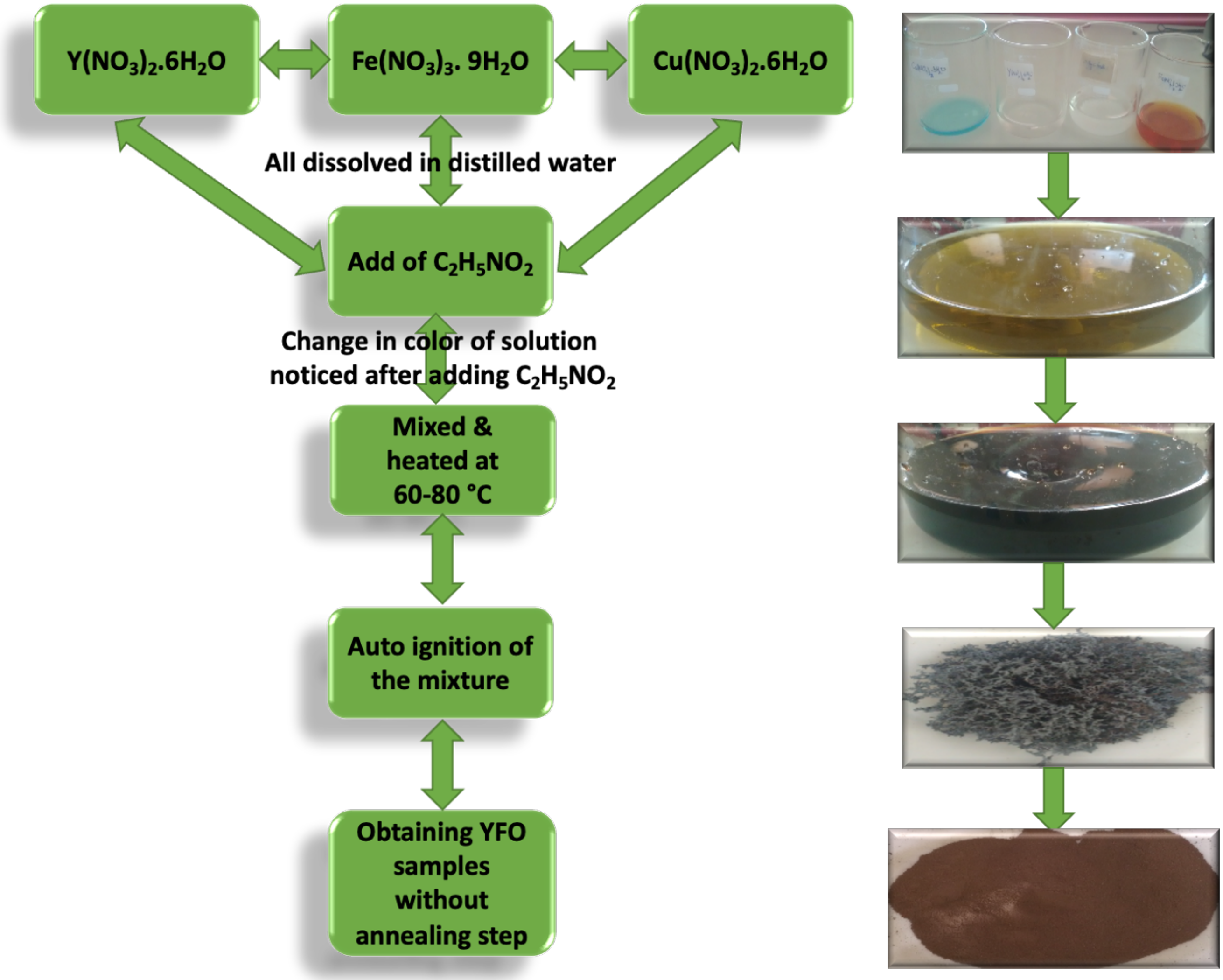

Fig. B.2.1: Chart of YFO preparation steps by the auto-combustion method.

- Photocatalysis application:

The photocatalytic activity of as-prepared samples was evaluated using a photochemical reactor (Techinstro, India) equipped with a 450W ultraviolet (UV) lamp and a visible reactor equipped with 500W Xenon (Visible) lamp. For this, 300 ml aqueous solution of methylene blue (0.02×10^{-3} mol/L) was taken in the reaction vessel followed by the addition of 0.1 g of YFO doped by Cu (x = 0, 0.1, 0.2, 0.3, and 0.4). Adsorption-desorption equilibrium of dye on the photocatalyst surface was ensured by magnetic stirring in dark for 20 min. The reaction medium is then subjected to UV and Visible light and the temperature was kept steady during the reaction using an external water circulatory chiller unit. The decrease in absorption values of MB solutions was continuously monitored at each 20 min time interval using a UV-visible spectrophotometer [2]. The degradation efficiency is calculated using the following equation:

Degradation of dye (%) = $[(C_0 - C_t) / C_0] \times 100\%$ (1)

$= [(A_0 - A_t) / A_0] \times 100\%$ (2)

Where C_0 and C_t are the initial and the final concentrations, respectively; A_0 and A_t is the corresponding absorbance values of MB, which were measured at the highest absorbance peak of MB of 665nm.

B.2.2. Results and discussion

B.2.2.a Structural characterization

The recorded Thermogravimetric Analysis spectra of non-annealed nanopowders $Y_{1-x}Cu_xFeO_3$ with Cu dopant percentage (0%, 10%, 20%, 30% & 40%) were shown in fig. 1 where the mass loss of the samples is not noticed as shown in table B.5, and the gain of weight due to the absorption of Nitrogen by the samples. Besides, TGA spectra showed that even at high temperatures there is no weight loss and no effect on all the samples [3, 4]. The increase in the intensity of peaks was related to the absorption N2 by YFO samples during the TGA test.

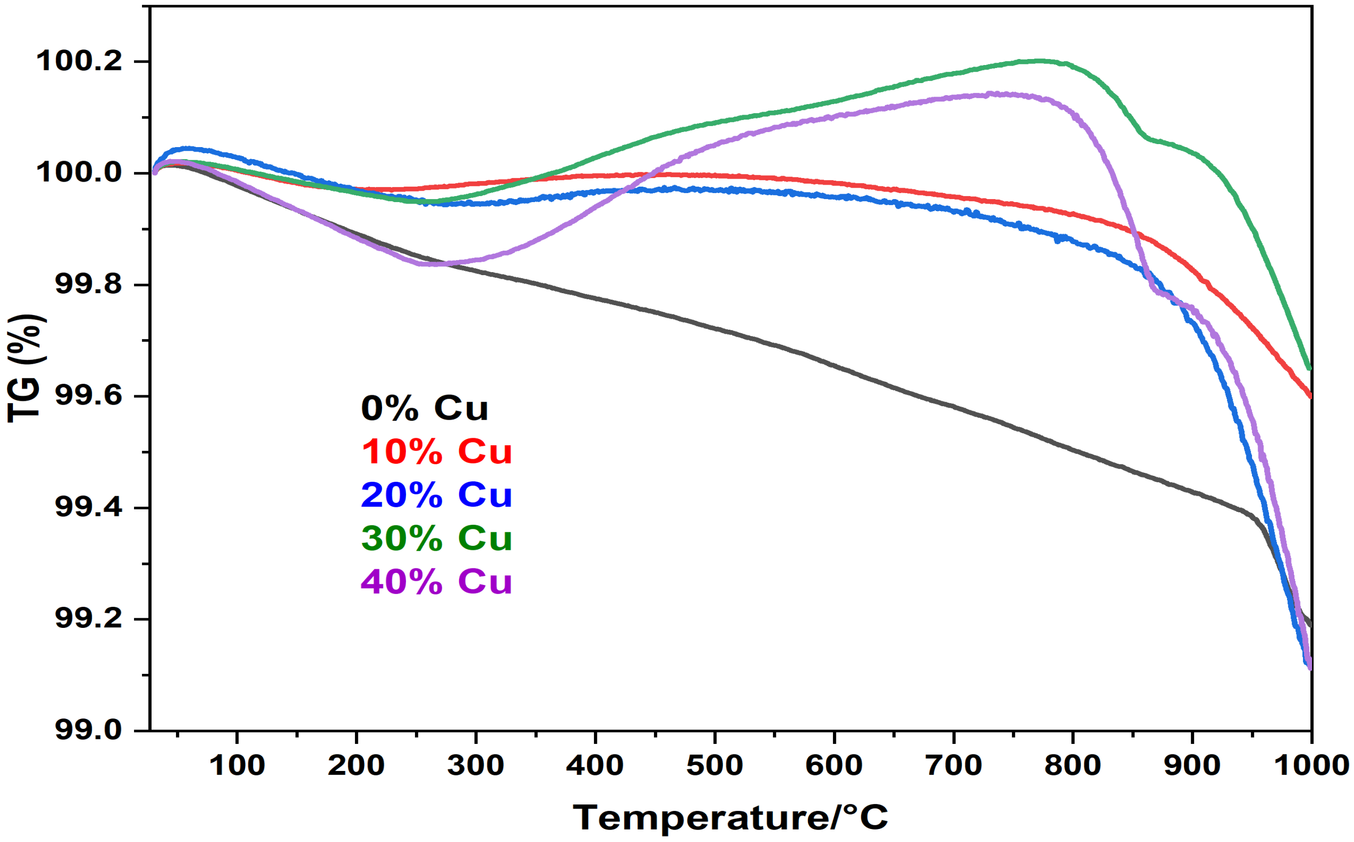

Fig. B.2.2 TGA spectra of the Cu-doped $YFeO_3$

Table B.2.1: Mass change of $Y_{1-x}Cu_xFeO_3$ nanopowders with Cu dopant percentage with the increase of temperature:

Samples of $Y_{1-x}Cu_xFeO_3$	Temperature range (°C)	Mass change (%)
x = 0	⇒ 0 – 300 ⇒ 300 – 950 ⇒ 950 – 1050	⇒ -0.19. ⇒ -0.44. ⇒ -0.19.
x = 0.1	⇒ 0 – 285 ⇒ 285 – 540 ⇒ 760 – 880	⇒ -0.07. ⇒ 0.15. ⇒ -0.15.
x = 0.2	⇒ 0 – 260 ⇒ 260 – 550 ⇒ 550 – 860 ⇒ 860 – 1050	⇒ -0.10. ⇒ 0.02. ⇒ -0.14. ⇒ -0.71.
x = 0.3	⇒ 0 – 260 ⇒ 260 - 515 ⇒ 760 – 885	⇒ -0.18. ⇒ 0.22. ⇒ -0.36.
x = 0.4	⇒ 0 – 230 ⇒ 230 – 500 ⇒ 825 – 1050	⇒ -0.05. ⇒ 0.03. ⇒ -0.31.

YFO nanocomposites were successfully synthesized by auto-combustion method by varying the Cu content from 10 to 50 % of $Y_{1-x}Cu_xFeO_3$ (x = 0, 0.1, 0.2, 0.3 & 0.4) which were represented in (Fig. 1a). The recorded X-ray diffraction patterns of non-annealed $Y_{1-x}Cu_xFeO_3$ nanopowders; where $0 \leq x \leq 0.4$, prepared by GNP were exhibited an orthorhombic structure o-$YFeO_3$ (JCPDS card no. 01-073-1345) with space group $Pbn2_1$ (no. 33) and unit cell parameters: a (Å) = 5.2819, b (Å) = 5.5957, c (Å) = 7.6046, angles: $\alpha = \beta = \gamma = 90°$ and volume of cell (10^6 pm^3) = 224.76, with no impurities for x = 0.2 and 0.3, and with two secondary phases: a cubic Yttrium oxide Y_2O_3 (JCPDS card no. 00-001-0831) with space group of $Ia\overline{3}$ at 2θ = 29.356 for x = 0, 0.1 and 0.4, and a Rhombohedral Yttrium Iron Garnet (YIG) $Y_3Fe_5O_{12}$ (JCPDS card no. 01-089-8185) with space group of $R\overline{3}$ (n0. 148) at 2θ = 35.538 for x = 0.4 only [4-7].

The average crystallite size of zinc ferrites compositions was calculated from the XRD spectra using the Debye-Scherrer formula [8, 9]

$$D = \frac{0.9\lambda}{\beta\cos\theta} \qquad (3)$$

where D is the crystalline size, λ denotes the wavelength of Cu-Kα X-ray radiation, β is the full width at half maximum of XRD peaks and θ is Bragg's angle. The variation of the crystal size of YFO compositions was plotted as a function of Cu dopant concentration as shown in Fig. 1b. It can be seen that subsequent changes in Cu content impose a slight variation of crystal sizes from 60 to 52 nm. While lower and higher doping concentrations (10%, 20%, 30% & 40% respectively) resulted in slightly lower crystal size, the lowest crystal size was obtained for higher Cu doping levels of 40% as shown in the following:

table B.2.2 Crystal size, unit cell parameters, and the volume cell.

Samples of $Y_{1-x}Cu_xFeO_3$	Crystallite size (nm)	Unit cell parameters (Å)			The volume of Cell (10^6 pm^3)
		a	b	c	
x = 0	55.45	5.300749	5.60778	7.631067	226.8368
x = 0.1	59.55	5.298473	5.605215	7.628707	226.5656
x = 0.2	56.38	5.176632	5.557461	7.626668	219.4111
x = 0.3	53.34	5.29263	5.597378	7.214279	225.5719
x = 0.4	51.59	5.281444	5.593516	7.604745	224.6582

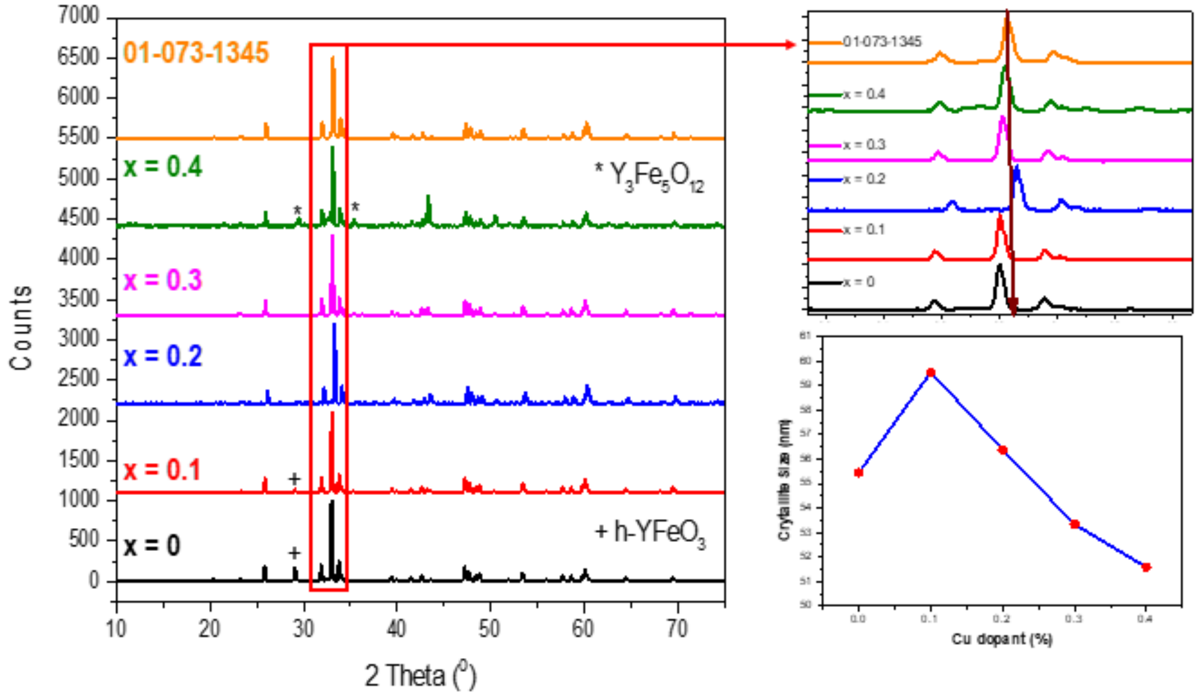

Fig. B.2.3 On left: XRD pattern of $Y_{1-x}Cu_xFeO_3$ powder as a function of Cu doping (x=0, 0.1, 0.2, 0.3, and 0.4) and on right: Plot of crystal size versus Cu dopant concentration.

Raman shifts spectra of $Y_{1-x}Cu_xFeO_3$ powder as a function of Cu doping percentage 10%, 20%, 30% & 40% were represented in fig. B.11.a $YFeO_3$ with a perovskite structure has 60 optical irreducible phonon modes of are as follows:

7A1g+8A1u+7B1g+8B1u+5B2g+10B2u+5B3g+10B3u

Only 24 of these modes (7A1g+5B1g+7B2g+5B3g) are active. FeO_6 octahedra have a vibration mode of around 221 cm^{-1} (A1g). Other peaks are associated with Fe-O bonds (281 cm^{-1} (B1g), 344 cm^{-1} (B2g), 430 cm^{-1} (A1g), 498 cm^{-1} (B3g), and Y-O bonds (156 cm^{-1} (A1g) and 186 cm^{-1} (A1g)). Because orthorhombic YFeO3 is the main phase and the marked diamond shape is related to Y-O bonds, where the hexagonal $YFeO_3$ has a marked heart shape, which is consistent with the literature, and the marked heart shape is related to Fe-O bonds in the Fe2O3, but these phases are minor and the fraction is relatively low. The peak at 1301 cm^{-1} is associated with the vibration of magnetic Fe^{3+} ions, which is consistent with previous studies for $YFeO_3$ powders and ceramics [10].

The FTIR spectra of $Y_{1-x}Cu_xFeO_3$ prepared nanopowders by auto combustion process were represented in Fig. B.11.b. The absorption bands' peaks are visible between 600 and 400 cm^{-1}. A sharp band has been observed in both spectra around 555 cm^{-1} and 563 cm^{-1}, respectively, which occurs due to the stretching of metal-oxygen (Fe–O) bonds in Perovskite-based materials. The remaining intense bands between 600 and 400 cm^{-1} can also be attributed to metal-oxygen vibrational bending in the garnet structure's dodecahedral units [11].

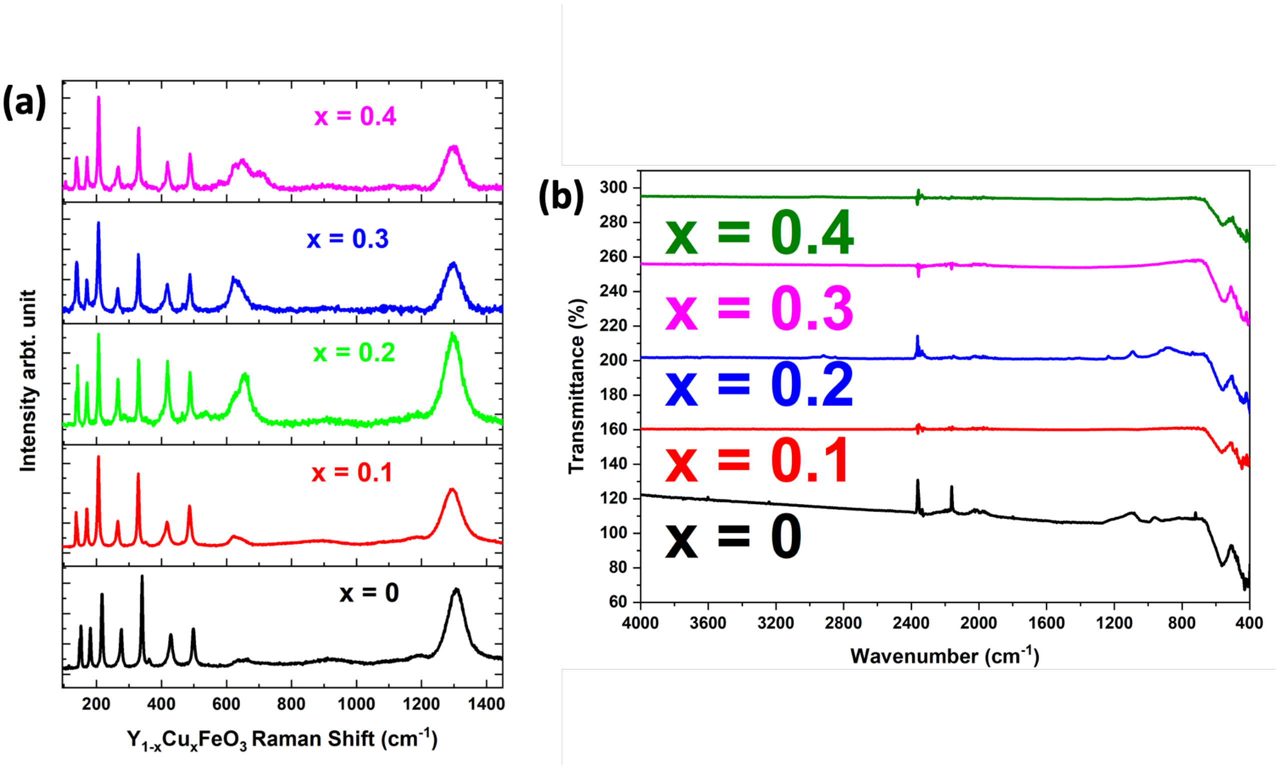

Fig. B.2.4 (a) Raman Shifts of $Y_{1-x}Cu_xFeO_3$ powder as a function of Cu doping percentage 10%, 20%, 30% & 40% (b) Fourier Transformation Infra-Red spectra of $Y_{1-x}Cu_xFeO_3$ powder as a function of Cu doping (x=0, 0.1, 0.2, 0.3, and 0.4).

B.2.2.b Morphological analysis:

The SEM images represented in fig B.12 were showing nanoparticles in the scale range of 31 to 140 nm, the grain size was increasing respectively with the increase of Cu dopant percentage. Also, there is a clear agglomeration in all samples due to the preparation process used as a minor effect and the nature of the as-prepared samples as a major effect because the agglomeration in Yttrium ferrite as-prepared samples is common due to the high magnetic properties of YFO samples, but it was noticed that the agglomeration was decreasing with the increase of Cu content (0%, 10%, 20%, 30% & 40%) due to the effect of doping which can lead to the decrease of the magnetic properties of the as-prepared YFO samples [10, 12].

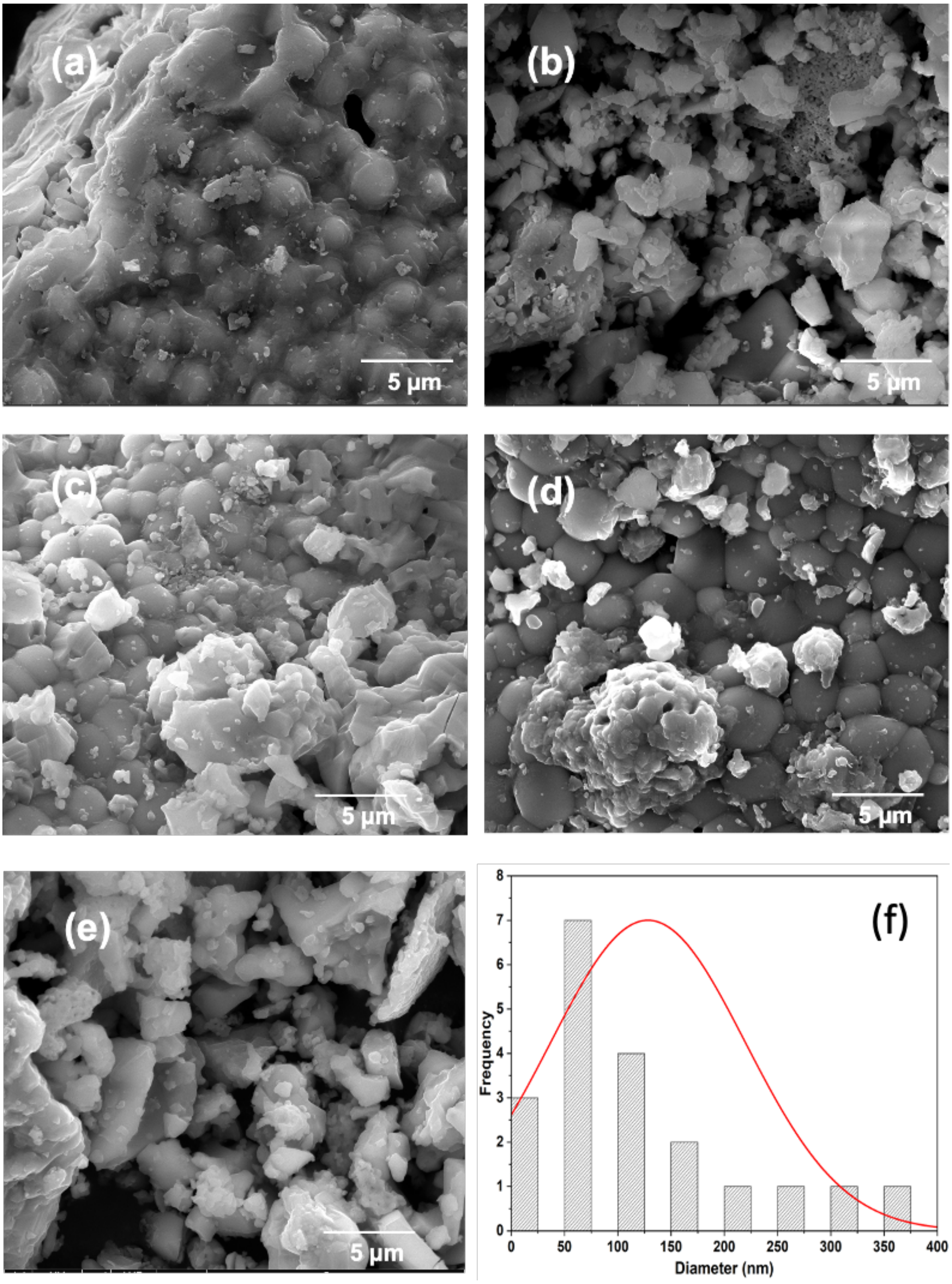

Fig. B.2.5 FESM images of $Y_{1-x}Cu_xFeO_3$ nanopowders with Cu dopant varaition; (a) 0%, (b) 10%, (c) 20%, (d) 30%, (e) 40%, & (f) Diameter histogram of 0% YFO.

B.2.2.c Photocatalysis application:

The photocatalytic activity of YFO samples was recorded after 140 min then represented in fig. B.13 where the degradation of Methylene blue was achieved under UV and Visible light for all the Cu-doped $YFeO_3$ as-prepared samples with the variation of Cu doping content from 0% to 40%. The adsorption-desorption reaction between the electrons, the radicals, and the dye led to the degradation of Methylene Blue by the photocatalyst YFO.

The normalized absorbances for YFO samples (A by A_0) under UV and Visible light were shown in fig. B.13. (a & b), from the spectra; it is clear that MB solution was degraded under Visible light better than under UV light. However, in fig. B.13. (c), the comparison between the nano-oxides degradation efficiencies under UV & Visible light were shown where the highest degradation efficiency was approximately 95% for 20% Cu content under visible light but under UV light was equal to 94% for 0%, 20% & 30% Cu content. Also, fig. B.13. (d) represented the kinetic constants of the as-prepared YFO samples, where $2x10^{-2}$ was the highest value for pure Yttrium ferrite ($YFeO_3$) then $1.7x10^{-2}$ for 20% Cu under Visible light, however the highest value under UV light was for 20% Cu $1.5x10^{-2}$.

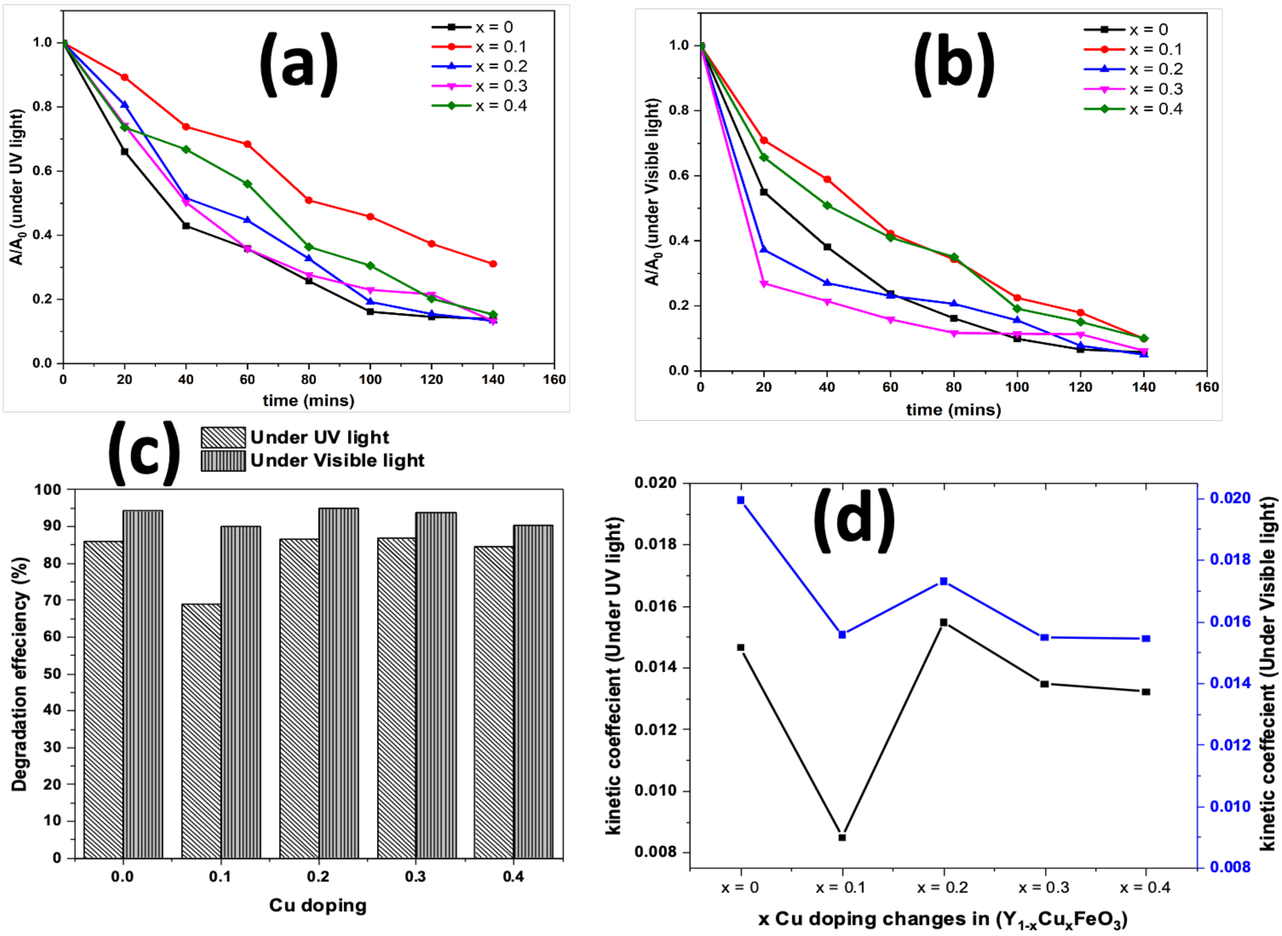

Fig. B.2.6 photocatalysis data for $Y_{1-x}Cu_xFeO_3$ nanopowders with Cu dopant varaition from 0 to 40% (a) Normalized absorbance (A by A_0) under UV light, (b) Normalized absorbance (A by A_0) under Visible light, (c) Degradation efficiency of YFO samples under UV & visible light, (d) Kinetic constant under UV & visible light.

Degradation of MB solution by Cu-doped YFO as-prepared samples was related to the crystallite size of the photocatalysts and Cu doping content percentage represented in Fig. B.14 (a), where the crystal sizes were varied from 52 to 60 nm randomly not related increasingly to the Cu dopant percentage for YFO samples. However, fig. B.14 (b) was showing the band gap for Cu-doped YFO photocatalysts; the band gap was slightly decreasing by the increase of Cu dopant % from 1.81 to 1.2 eV showing the strong visible activity of the samples that was enhanced up to 20% Of Cu dopant then decreased again. In addition, fig. B.14 (c) represented the degradation efficiency of MB solution degraded by 20% Cu dopant with band gap of 1,38 eV: under sunlight (D%= 26%), under Visible light (D%= 94%), and under UV light (D%= 95%). Finally, the recyclability of 20% Cu-doped YFO was investigated under Visible light for 3 cycles and the degradation efficiencies were showing in fig. B.14 (d) the ability of the reusability of the photocatalyst to degrade the pollutant for three successive repeated cycles. The recyclability of 20% Cu-doped $YFeO_3$ after 3 times where the degradation efficiency at the 3rd cycle was equal to ~19% due to the hard recovery of the sample from the solution because of the high magnetic properties that made the sample around the magnet.

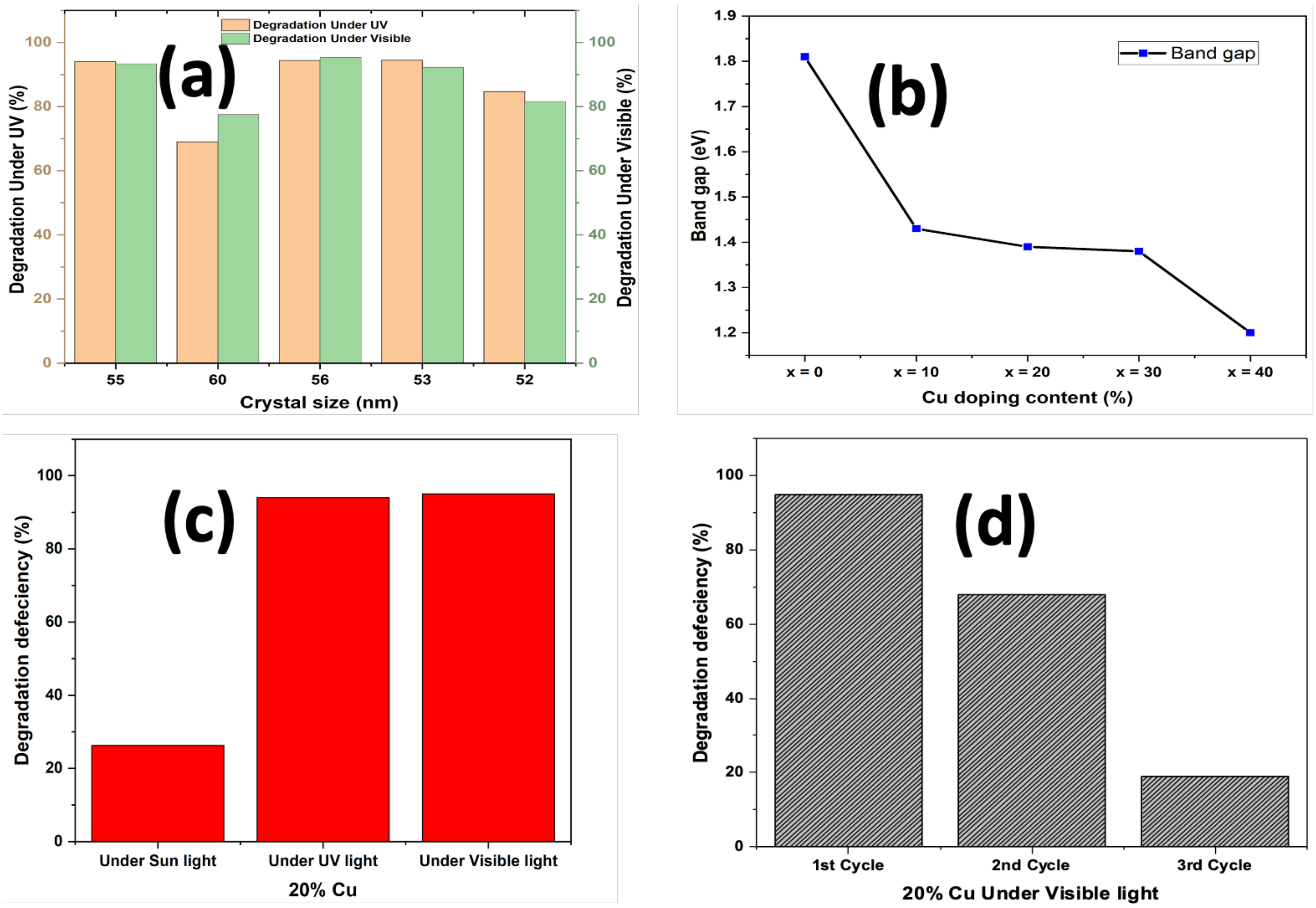

Fig. B.2.7 (a) Crystal size versus degradation efficiency of MB solution by YFO as-prepared samples, (b) Band gap of YFO by Cu doping content percentage, (c) Degradation efficiency of 20% Cu-doped YFO under sun light, UV light, & Visible light, (d) Recyclability panels for 20% Cu-doped YFO samples under Visible light.

Fig. B.15 represented the suggested photocatalytic mechanism of Methylene Blue removal under UV irradiation and Visible light for all the nanosized Cu-doped $YFeO_3$ samples (0%, 10%, 20%, 30% & 40%), where under sunlight was investigated only for 20% Cu-doped $YFeO_3$ sample. The interactions between the electrons of YFO photocatalysts, the radicals, and the ions played a big role in degrading the dye. In addition, YFO nano oxides absorb sufficient energy to excite electrons from the valence band (VB) to the conduction band (CB), resulting in free electrons (e-) in the CB and holes (h+) in the VB in order to be released in the MB aqueous solution to react with the dissolved oxygen in the medium to form superoxide radicals (O^{2-}) [13, 14]. These can then attack water molecules or hydroxyl ions to produce reactive hydroxide ions ($OH^{\cdot}$) capable of attacking dye molecules [15] leading to the decomposition of the organic dye into nontoxic intermediates products such as CO_2 and H_2O due to the formation of promoted OH radicals and the presence of h+ in the valence band. The photogenerated $OH^{\cdot}$, e^-, and h^+ were the main active elements of $YFeO_3$ for the degradation of the organic pollutant MB under Visible and UV light.

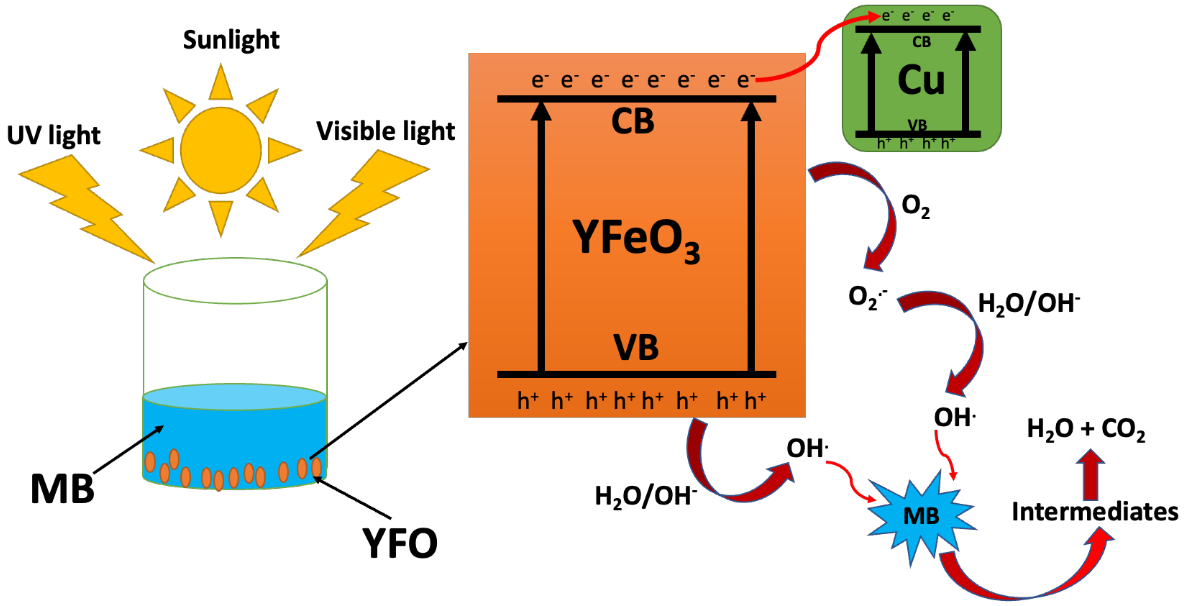

Fig. B.2.8 Suggested mechanism of photocatalytic removal for Methylene blue by YFO nanophotocatalysts.

We have compared the results of our Cu-doped YFO samples with previous investigated works of YFO tests for photocatalytic activity under UV & Visible light to study the effect of Cu doping on the degradation efficiency of Methylene Blue shown in (table B.4).

Table B.2.3: as-prepared YCFO compared with previous studies in degradation efficiency.

Photocatalyst material	Dye	Irradiation light	Irradiation time (min)	Degradation effeciancy (%)	Earlier reports
$YFeO_3$	Rhodamine B	Visible	120	70	Tang, Peisong, et al. (2011) [17]
$YFeO_3$	Methyl Orange	Visible	120	90	Tang, Pei Song, et al. (2015) [18]
$LaFeO_3$	Methylene Blue	Visible	60	100	Tang, Peisong, et al. (2013) [19]
Er^{3+}: $YFeO_3/TiO_2$-SAC	Methyl Orange	Visible	80	92	Hou, Dianxun, et al. (2012) [20]
$Y_{1-x}Bi_xFeO_3$	Methylene Blue	Visible	240	80	Rosales-González, O., et al. (2020) [21]
$YFeO_3$	Methyl Orange	Visible	300	95	Zhang, Yuewei, et al. (2014) [22]
$YFeO_3$/Carbon fiber	Reactive Black 5	Visible	60	99	Liu, Yi-Hung, et al. (2021) [23]
$YFeO_3$/Carbon fiber	Reactive Black 5	UV	120	50	Liu, Yi-Hung, et al. (2021) [23]
$Y_{1-x}Cu_xFeO_3$	Methylene Blue	Visible	140	95	Current work
$Y_{1-x}Cu_xFeO_3$	Methylene Blue	UV	140	94	Current work

B.2.3. Conclusions

In summary, the non-annealed YFO nanomaterials with varying Cu dopants were successfully synthesized using the auto-combustion process. XRD revealed the formation of Yttrium ferrites crystallites with orthorhombic Perovskite structure. The morphology of different YFO nano-oxides was evaluated using SEM. The degradation rate of MB solution was investigated under UV and Visible light and the highest degradation efficiency was 95% for 20% Cu doping percentage. The reusability of the photocatalyst was achieved up to the second cycle.

References

1. Hwang, C.-C., J.-S. Tsai, and T.-H. Huang, Combustion synthesis of Ni–Zn ferrite by using glycine and metal nitrates—investigations of precursor homogeneity, product reproducibility, and reaction mechanism. Materials Chemistry and Physics, 2005. 93(2-3): p. 330-336.
2. Gaidi, M., et al., Enhanced photocatalytic activities of silicon nanowires/graphene oxide nanocomposite: Effect of etching parameters. Journal of Environmental Sciences, 2020. **101**: p. 123-134.
3. *Xu, H., Yan, H., & Chen, Z. (2006). Mechanism of Citric Acid-Nitrates Low-Temperature Combustion for Ce~ 0~.~ 8Y~ 0~.~ 2O~ 1~.~ 9 Nano-Scale Powders. JOURNAL-CHINESE CERAMIC SOCIETY, 34(4), 393.*
4. *Wang, J., Li, C., & Xu, B. (2009). Basic principle, advanced and current application situation of sol-gel method. Chem Ind Eng, 26, 273-277.*
5. Wu, L., Jimmy, C. Y., Zhang, L., Wang, X., & Li, S. (2004). Selective self-propagating combustion synthesis of hexagonal and orthorhombic nanocrystalline yttrium iron oxide. Journal of Solid State Chemistry, 177(10), 3666-3674.
6. Gil, D. M., Navarro, M. C., Lagarrigue, M. C., Guimpel, J., Carbonio, R. E., & Gómez, M. I. (2011). Synthesis and structural characterization of perovskite YFeO 3 by thermal decomposition of a cyano complex precursor, Y [Fe (CN) 6]· 4H 2 O. Journal of thermal analysis and calorimetry, 103(3), 889-896.
7. Popkov, V. I., Almjasheva, O. V., & Gusarov, V. V. (2014). The investigation of the structure control possibility of nanocrystalline yttrium orthoferrite in its synthesis from amorphous powders. Russian Journal of Applied Chemistry, 87(10), 1417-1421.
8. Meng, W., et al., Photocatalytic activity of highly porous zinc ferrite prepared from a zinc-iron (III)-sulfate layered double hydroxide precursor. Journal of Porous Materials, 2004. 11(2): p. 97-105.
9. Phumying, S., et al., Nanocrystalline spinel ferrite (MFe2O4, M=Ni, Co, Mn, Mg, Zn) powders prepared by a simple aloe vera plant-extracted solution hydrothermal route, Mater. Res. Bull. 2013. 48: p. 2060-2065.
10. *Wang, M., Wang, T., Song, S. H., Ravi, M., Liu, R. C., & Ji, S. S. (2017). Effect of calcination temperature on structural, magnetic and optical properties of multiferroic YFeO3 nanopowders synthesized by a low temperature solid-state reaction. Ceramics International, 43(13), 10270-10276.*
11. *Suthar, L., Bhadala, F., & Roy, M. (2019). Structural, electrical, thermal and optical properties of YFeO3, prepared by SSR and sol–gel route: a comparative study. Applied Physics A, 125(7), 1-8.*
12. *Popkov, V. I., Almjasheva, O. V., Nevedomskiy, V. N., Panchuk, V. V., Semenov, V. G., & Gusarov, V. V. (2018). Effect of spatial constraints on the phase evolution of YFeO3-based nanopowders under heat treatment of glycine-nitrate combustion products. Ceramics International, 44(17), 20906-20912.*
13. *Malato, S.; Fernandez-Ibanez, P.; Maldonado, M.I.; Blanco, J.; Gernjak, W. Decontamination and disinfection of water by solar photocatalysis: Recent overview and trends. Catal. Today 2009, 147, 1–59.*
14. N. Barsan et al, Metal oxide-based gas sensor research: How to?, Elsevier, 2006

15. *Mills, A.; Le Hunte, S. An overview of semiconductor photocatalysis. J. Photochem. Photobiol. A 1997, 108, 1–35.*
16. *Tang, P., Chen, H., Cao, F., & Pan, G. (2011). Magnetically recoverable and visible-light-driven nanocrystalline YFeO 3 photocatalysts. Catalysis Science & Technology, 1(7), 1145-1148.*
17. *Tang, P. S., Tang, C. W., Ying, J. N., Ni, D. J., Yang, Q., & Wu, L. M. (2015). Preparation of nanoparticulate YFeO3 by ultrasonic assisted method and its visible-light photocatalytic properties. In Key Engineering Materials (Vol. 636, pp. 7-10). Trans Tech Publications Ltd.*
18. *Tang, P., Tong, Y., Chen, H., Cao, F., & Pan, G. (2013). Microwave-assisted synthesis of nanoparticulate perovskite LaFeO3 as a high active visible-light photocatalyst. Current Applied Physics, 13(2), 340-343.*
19. *Rosales-González, O., Sánchez-De Jesús, F., Camacho-González, M. A., Cortés-Escobedo, C. A., & Bolarín-Miró, A. M. (2020). Synthesis of magnetically removable photocatalyst based on bismuth doped YFeO3. Materials Science and Engineering: B, 261, 114773.*
20. *Hou, D., Feng, L., Zhang, J., Dong, S., Zhou, D., & Lim, T. T. (2012). Preparation, characterization and performance of a novel visible light responsive spherical activated carbon-supported and Er3+: YFeO3-doped TiO2 photocatalyst. Journal of hazardous materials, 199, 301-308.*
21. Zhang, Y., Feng, J., Xu, J., Chen, G., & Hong, Z. (2014). Solvothermal Synthesis and Visible-Light Driven Photocatalytic Properties of YFeO3 Nanoparticles. *Integrated Ferroelectrics*, *151*(1), 108-115.
22. *Zhang, Y., Feng, J., Xu, J., Chen, G., & Hong, Z. (2014). Solvothermal Synthesis and Visible-Light Driven Photocatalytic Properties of YFeO3 Nanoparticles. Integrated Ferroelectrics, 151(1), 108-115.*
23. Liu, Y. H., Kuo, Y. S., Liu, W. C., & Chou, W. L. (2021). Photoelectrocatalytic activity of perovskite YFeO3/carbon fiber composite electrode under visible light irradiation for organic wastewater treatment. *Journal of the Taiwan Institute of Chemical Engineers*, *128*, 227-236.

General Conclusion

Conclusion

In conclusion, the semiconductors Zinc and Yttrium ferrites are used as photocatalysts for water treatment application for the removal of Methylene Blue; the well-known organic pollutant dye, from the environment.

- For Zinc ferrites, the nanocomposites were prepared by the auto combustion method and annealed at 1000 °C then investigated by different characterization methods which proved the formation of Zinc ferrite spinel structure and its crystallinity. Moreover, SEM evaluated its morphology and the photocatalytic behavior showed the recyclability of as-prepared Zin ferrite up to three cycles:
    - XRD for the annealed samples of Ni-doped $ZnFe_2O_4$ were showing the pure Zin ferrite peaks with extra peaks of other phases were presented such as $(Ni,Zn)ZnFe_2O_4$,Fe_2O_3 and ZnO.
    - Raman & FTIR supported XRD results and confirmed the formation of ZFO perovskite oxide.
    - SEM images showed that the grain size of ZFO samples was found to be in the range of 103 to 766 nm for different compositions from 0% up to 60% of Ni doping content percentage
    - Raman shifts and IR specters confirmed the formation of ZFO with spinel oxide structure supporting the XRD data.
    - The photocatalytic activity tests for the Ni doped ZFO samples (0% to 60%) showed the photocatalysis properties of the nanomaterial under UV light with an optimum of 98% for 30% Ni content percentage. Herein, the recyclability of the nanophotocatalyst was achieved up to the third cycle with value of 85%.
- For Yttrium ferrites, the nano oxides were prepared by the auto combustion process and investigated by different characterization methods which proved the formation of

Yttrium ferrite Perovskite structure and its crystallinity. In addition, SEM evaluated its morphology where and the photocatalytic behavior showed the recyclability of the non-annealed as-prepared Yttrium ferrite up to three cycles:

- XRD for non-annealed samples of $Y_{1-x}Cu_xFeO_3$ showed the formation of the orthorhombic $YFeO_3$ peaks with extra peaks of other phases such as hexagonal $YFeO_3$ and Garnet $Y_3Fe_5O_{12}$. The crystallite size from 52 to 60 nm proved the nano size of the YFO samples.
- Raman & FTIR supported XRD results and confirmed the formation of YFO perovskite oxide.
- The SEM images for YFO samples were showing nanoparticles in the scale range of 31 to 140 nm, the grain size was increasing respectively with the increase of Cu dopant percentage.
- The photocatalytic activity study confirmed that Cu-doped YFO Perovskite oxides (0% to 40%) can be a good photocatalyst under UV & Visible light where the optimum degradation efficiency with value of 95% under Visible light. Also, the reusability under Visible light of the nanomaterial of 20% Cu was confirmed up to third cycle with value of 19%.

Abstract

In summary, ZFO nanocomposites with varying Ni dopants were successfully synthesized using auto-combustion followed by the annealing process. XRD revealed the formation of zinc ferrites crystallites with cubic spinel structure. The morphology of different zinc ferrites was evaluated using SEM. The degradation rate of MB solution increases successively with Ni doping up to 30% and thereafter decreases. With an optimum Ni doping (30%), photocatalytic activity up to 98% was achieved with as-synthesized ZFO nanocomposites, which can perform as an environmentally friendly, easily isolable, and recyclable photocatalyst for water treatments.

Moreover, the non-annealed YFO nanomaterials with varying Cu dopants were successfully synthesized using the auto-combustion process. XRD revealed the formation of Yttrium ferrites crystallites with orthorhombic Perovskite structure. The morphology of different YFO nano-oxides was evaluated using SEM. The degradation rate of MB solution was investigated under UV and Visible light and the highest degradation efficiency was 95% for 20% Cu doping percentage. The reusability of the photocatalyst was achieved up to the third cycle.

Keywords: ZFO, YFO, Ni-doped, Cu-doped, photocatalysis, photocatalyst MB, nanomaterials.

ملخص

باختصار، تم توليف مركبات (YFO) النانونية بنجاح و ذلك بإضافة نسب متفاوتة من النيكل باستخدام تفاعل الاحتراق الذاتي متبوعا بعملية التلدين. تم التحقق من تشكل بلورات زنك الحديد ذات الهياكل المكعبة الورانية عن طريق (XRD). و كذلك (SEM) كشف لنا مختلف البنيات المتواجدة في (ZFO). سرعة تحلل محلول أزرق البروموتيمول ازدادت بنجاح مع ازدياد نسبة إضافة النيكل حتى ٣٠٪ و بعدها نقصت. تم التأكد من نشاط التحليل الكهروضوئي حتى نسبة ٩٨٪ بالنسبة ل٣٠٪ من النيكل المضاف إلى المركبات النانونية ل (ZFO) و التي تم تحضيرها كي تكون كمواد صديقة للبيئة، سهلة العزل، و يمكن إعادة تدويرها لمعالجة المياه.

علاوة على ذلك، تم توليف مواد نانونية (YFO) بتراكيز مختلفة من عنصر النحاس باستخدام عملية الاحتراق الذاتي بدون تلدين. تم التحقق من تشكل بلورات إيتريوم الحديد ذات هياكل البيروفسكيت الأورثورمبية ب(XRD). و (SEM) قيمت شكل مختلف بنيات (YFO). تم دراسة سرعة تحلل محلول أزرق البروموتيمول تحت الضوء فوق البنفسجي و الضوء المرئي، و أعلى كفاءة تحلل كانت ٩٥٪ لنسبة ٢٠٪ من النحاس المضاف. تم النجاح في إعادة استخدام المحفز الضوئي حتى المرة الثالثة.

الكلمات المفتاحية: أكسيد زنك الحديد، أكسيد إتيريوم الحديد، إضافة النيكل، إضافة النحاس، التحليل الكهروضوئي، محفز التحليل الضوئي، أزرق البروموتيمول، المواد النانوية.